



# Particle Impact Characteristics Influence on Cold Spray Bonding: Investigation of Interfacial Phenomena for Soft Particles on Hard Substrates

A. Nastic<sup>1</sup> · B. Jodoin<sup>1</sup> · J.-G. Legoux<sup>2</sup> · D. Poirier<sup>2</sup>

Submitted: 30 July 2021 / in revised form: 21 October 2021 / Accepted: 25 October 2021 / Published online: 22 November 2021  
© ASM International 2021

**Abstract** The influence of particle impact temperature and size on adhesion of soft particle/hard substrate material in cold spray has been scarcely studied. While the relationship between particle impact conditions and particle/substrate bonding is commonly established through FEM studies, they typically lack comparison to experimental data. In the current study, characterization was performed by post-mortem observation of removed adhered particles and collected rebounded particles contact surfaces. Observations are correlated to interfacial pressure and temperature using FEM, otherwise impossible to measure in situ. The influence of pressure and its temporal evolution with particle deformation on melting and bonding is evaluated. Evidence of anisotropic particle deformation associated with microstructural orientation and grain geometrical features has been observed. Experimental evidence confirms that the particle south pole experiences restricted deformation as the original powder grain morphology was observed even after impact. Interfacial melt features have been detected and the melt zone generation, propagation, stagnation and regression tracked through FEM have shown important influence on single impact adhesion processes. Observed metallic bonding features and FEM indicate that increasing particle velocity, i.e., decreasing particle size, accelerates particle bonding processes to occur within tens of nanoseconds. Contact compressive

pressure and interfacial expansion increase with particle increasing velocity and temperature.

**Keywords** impact temperature · melt front · metallic bonding · oxide layer · peening · pressure-dependent melting

## Introduction

The cold gas dynamic spray (CGDS) process accelerates micron-size particles to high velocities (400–1000 m/s), using a supersonic gas flow. After exiting the nozzle, the high-speed particles impact a target surface generating localized material heating and cooling rates up to  $10^9$  K/s, strain levels above 10 and strain rates up to  $10^9$  s<sup>-1</sup>. These impact phenomena lead to physical/chemical processes, such as melting (Ref 1, 2), phase transformation (Ref 3), amorphization (Ref 4), jetting (Ref 5), oxide layer fragmentation (Ref 6), twinning (Ref 7) and most importantly atomic (also often referred to as metallurgical or metallic) bonding (Ref 8).

It is widely accepted that solid-state atom-to-atom bonding requires oxide-free clean surfaces to be put in contact under high localized pressure (Ref 9, 10). Finite element modeling (FEM) has been used to confirm these findings and visualize the bonding process during impact, as the process length (microns) and time (nanoseconds) scales prevent experimental measurements during CGDS (Ref 11–14). Evidence of metallic bonding at particle/substrate interfaces has been mostly based on cross-sectional interface examinations, which have shown that the metallurgically bonded zone is almost always ring-shaped, between the particle south pole and the location of jetted material (Ref 15–18).

✉ A. Nastic  
anast064@uottawa.ca

<sup>1</sup> University of Ottawa Cold Spray Laboratory, Ottawa, ON, Canada

<sup>2</sup> National Research Council of Canada, Boucherville, QC, Canada

Most studies have focused on the analysis of metallurgical bonding occurrence and features for particle/substrate of similar mechanical properties, referred to as hard/hard and soft/soft material pairs (Ref 2, 6, 8, 17, 19–22). Material combinations with comparable hardness to elastic modulus ratio inevitably include concurrent interfacial mechanical and metallurgical bonding mechanisms for which the separate effects on adhesion are hardly dissociable. However, for soft particle/hard substrate material pairs, the substrate deformation is limited, and mechanical anchoring is negligible. This limited substrate deformation restricts proper native oxide layer removal and fresh-metal contact impeding the creation of metallic bonds. For such material pair, studies have demonstrated that increasing substrate temperature can improve its deformation enough to enhance metallic adhesion without generating mechanical anchoring (Ref 23–25). Nevertheless, the study of substrate preheating on particle bonding is limited (Ref 26). Similarly, the influence of particle impact temperature on adhesion for soft/hard material pair is scarce. The reported benefits of increasing particle temperature in similar material combinations, such as the rise in interfacial temperature promoting thermally softened zones, deformation, oxide fracture, atomic mixing and consequently bonding (Ref 27–30), might not be relevant to the soft/hard material pair. An increase in particle temperature would only accentuate further the particle deformation without significant change to the substrate plastic flow.

A study on particle impact temperature influence on coating adhesion strength has reported that soft aluminum deposited under cold particle impact temperatures on hard steel provided increasing strengths with increasing particle size (Ref 31). This rise in bonding has been predominantly associated with the increasing in situ peening frequency of cold particles bouncing off instead of bonding to the substrate with increasing particle size. The in situ peening was correlated with coating deposition efficiency (DE), which has shown to be very low for cold impact temperatures, i.e., 5 to 13 %, and declining with increasing particle size (Ref 17, 31). In comparison, for particles reaching the substrate at a higher impact temperature, the coating adhesion strength rises with particle decreasing size. The heated particles allowed an important increase in deposition efficiency, i.e., 50 to 90 %, which has shifted the bonding mechanism to particle impact characteristics (velocity and temperature) rather than in situ peening. While these results contribute to the understanding of soft/hard material bonding processes, the influence of particle impact temperature on interfacial features and bonding processes at the individual particle level has not been studied.

Consequently, the aim of the current study is to analyze the effect of particle impact temperature and size on impact characteristics and adhesion strength for the soft/hard

material combination at the individual particle level. Spherical aluminum particles of varying size are deposited at low and high impact temperature, while maintaining a similar impact velocity, on a hard steel substrate material. The current study provides a detailed characterization of interfacial phenomena based on particle size and impact temperature. Adhered particles are removed from the substrate, and the fracture surfaces are examined to characterize the metallurgical bonding zones size, geometry, and location. Rebounded particles are collected, and their surfaces analyzed. In addition, FEM is used to correlate the experimental observations to interfacial characteristics (pressure and temperature).

## Experimental Procedures

### Feedstock Powder

The feedstock powder used is a commercially available pure aluminum powder (Equispheres, ON, CA). The powder manufacturing process produces solely spherical particles, as shown in Fig. 1(a), (b) and (c). This eliminates/reduces the geometrical effects related to teardrop and irregular powder shapes (Ref 12, 32), such as generation of particle angular momentum, unclear initial impact contact point and untraceable original geometry. In addition, the three distinct aluminum powder diameter ranges, as depicted in Fig. 1(a), (b) and (c), allow a size-dependent study. The average diameters are 40  $\mu\text{m}$ , 58  $\mu\text{m}$  and 68  $\mu\text{m}$  for set 1, set 2 and set 3, respectively.

Equiaxed, dendritic and columnar grains surface microstructures, shown in Fig. 1(d), (e) and (f), are observed in all three particle size sets. These microstructural variations result from directional solidification, heterogeneous nucleation sites, particle to particle contact and cooling rate during manufacturing (Ref 33–35). The solidification rates can differ between the particle external shell and interior bulk material (Ref 34, 35). In the current study, as shown in Fig. 1(g), (h) and (i), the microstructure is uniform throughout the particle suggesting homogeneous solidification rates. The same grain types are also detected in the etched powder cross sections.

Since loss in ductility and lack of metallic bonding is usually observed with the presence of oxide dispersion and oxide surface layer, respectively, an elemental analysis focusing on oxygen detection has been conducted for all powder sets. The powder oxygen concentration has been measured using an oxygen analyzer (Leco ONH836, MI, USA) through the inert gas fusion (IGF) method following the ASTM E 1019-03 standard. According to the analysis, presented in Table 1, the oxygen concentration in the powder set 1 (smallest size range) is almost twice the

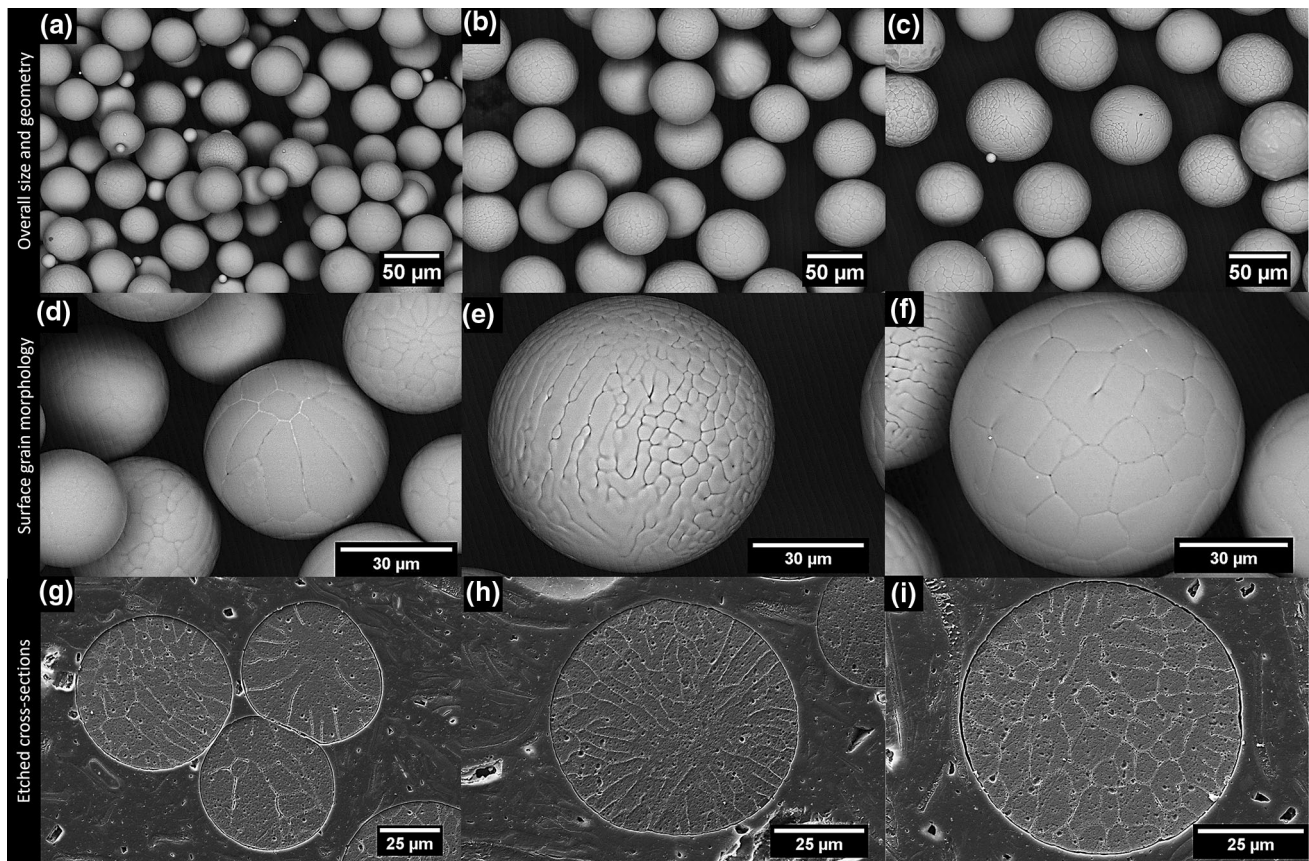


**Fig. 1** Backscattered electron images of powders with diameter range between (a) 13–48 μm with scarce powder below 13 μm (set 1), (b) 48–63 μm (set 2) and (c) 53–76 μm (set 3). (d–f) Types of surface morphologies observed through backscattered electron detector, i.e.,

equiaxed, dendritic and columnar grains, and detected in all three powder sets. Secondary electron analysis of powder cross-sectional grain morphology after etching with Keller’s solution (g–h–i)

**Table 1** Approximated surface oxide layer thickness (nm) calculated using measured total oxygen content through IGF method.

	38–45 μm	53–63 μm	63–75 μm
LECO (wt.%, thickness)	430 ppm/4.15 nm	240 ppm/3.36 nm	240 ppm/3.94 nm

concentration detected in set 2 and set 3. From these measurements, the surface oxide layer thickness has been approximated using the assumptions that the oxygen is confined to the particle surface and is of constant thickness (Ref 6);

$$\frac{V_{ox}\rho_{ox}}{V_{Al}\rho_{Al} + V_{ox}\rho_{ox}} = X_{ox(wt.\%)}, \tag{Eq 1}$$

where  $X_{ox}$  is the oxygen weight percent contribution to the Al-powder from the surface oxide scale,  $\rho_{ox}$  and  $\rho_{Al}$  are the aluminum oxide and pure aluminum densities, respectively, and  $V_{ox}$  and  $V_{Al}$  are the oxide shell and spherical pure aluminum volume, respectively.

The  $X_{ox}$  has been calculated using the measured oxygen concentration,  $O_c$ , as follow:

$$X_{ox(wt.\%)} = 1 - \left[ \frac{M_{Al}(Al_2O_3) \cdot O_c}{M_O(Al_2O_3)} + O_c \right], \tag{Eq 2}$$

where  $M_{Al}(Al_2O_3)$  and  $M_O(Al_2O_3)$  are the molecular weight of aluminum and oxygen in alumina, respectively.

Table 1 presents the measured oxygen content (ppm) along with the corresponding calculated oxide thickness. The alumina layer thickness is 4.15 nm, 3.36 nm and 3.94 nm for powder set 1, set 2 and set 3, respectively.

The mechanical response of particles has also been evaluated using an indenter equipped with a Berkovich tip. Fifteen indents per powder sets have been analyzed. The indentations have been performed at a peak load of 0.03 N, a dwell time of 15 s at the peak load and a loading/unloading rate of 0.017 N/s. As reported in Table 2, all three

**Table 2** Powder hardness measurement obtained using instrumented indentation.

	38–45 $\mu\text{m}$	53–63 $\mu\text{m}$	63–75 $\mu\text{m}$
Hardness	$393 \pm 39$ MPa	$368 \pm 59$ MPa	$385 \pm 50$ MPa

sets of powder have comparable hardness. Observed deviations are expected to be caused by grain size and grain geometry variations detected in the powders, as shown previously in Fig. 1, and by any epoxy damping during loading.

Since the oxide thickness values obtained through IGF approach values reported for aluminum powder using transmission electron microscopy (TEM) and x-ray photoelectron spectroscopy (XPS) (Ref 36), and that the hardness results are similar, it can be concluded that the oxygen is mostly confined to the particle surface, i.e., oxide film. This is a realistic assumption since in common aluminum powder manufacturing processes, such as gas atomization, the oxygen is predominantly bound to the surface (Ref 37).

### Substrate Material

Low carbon steel (SAE1018) has been used as substrate. Its hardness has been measured at  $90.5 \pm 0.3$  HRB. Substrate samples have been cut into cylinders (25.4 mm diameter and 40 mm height). Cold spray deposition was made on the flat ends, which have been polished to a mirror surface finish using  $3\mu\text{m}$  abrasive suspensions.

### Cold Spray Deposition

The deposition of individual particles is made through wipe tests. In these tests, the spray jet is moved at 150 mm/s, and with limited powder feed rate. Commercially available (SST-EP, CenterLine Limited, Windsor, ON, CA and Oerlikon Metco KINETIKS 4000, Schwyz, CH) CS systems have been used to achieve cold and hot particle impact temperatures for the same impact velocity. In the SST-EP system, a polymer nozzle with a 2.0 mm throat diameter, 6.4mm exit diameter and diverging length of 126 mm was utilized. The powder is injected radially, after the nozzle throat. A SiC nozzle with a 2.7 mm throat diameter, 6.96 mm exit diameter and 132 mm diverging length has been used in the KINETIKS 4000 system. The powder injection is located at the center of the converging nozzle section, without a pre-chamber, and oriented parallel to the nozzle axis. Prior to the deposition process, all substrates have been cleaned and degreased in ethanol.

The process gas stagnation parameters were set to obtain the same particle impact velocity for both systems. These velocities have been measured and reported in (Ref 31). Both systems used a gas stagnation temperature and pressure of 500 °C and 3.45 MPa, respectively. The standoff distance was set to 15 mm. Validated CFD models have been utilized in (Ref 31) to evaluate the particle impact temperature, velocity and critical velocities, which are reported in Table 3 for both low particle impact temperature (LPIT) sprays, obtained using the SST-EP system, and high particle impact temperature (HPIT) sprays, obtained using the KINETIKS 4000 system. As shown in Table 3 the critical velocity for HPIT ( $V_{C\_HPIT}$ ) is much lower than the one for LPIT ( $V_{C\_LPIT}$ ) sprays. This decrease results from the larger particle impact temperature for HPIT depositions, which allows higher deformation and improved oxide breakage and removal (Ref 31). The impact temperature reached by particles traveling at the corresponding critical velocities is referred to as  $T_L$  and  $T_H$  for LPIT and HPIT sprays, respectively, as presented in Table 3.

### Single Particle Deposition Analysis

The sprayed surfaces have been analyzed to characterize the interfacial phenomena generated by incoming particles. Rebounding particles have been collected during spray using a metal screen covered with double-sided carbon tape to allow the attachment of particles upon their contact with the screen, as illustrated in Fig. 2(a). Adhered particles have been pulled off from the substrate. As illustrated in Fig. 2(b) thermally curing elastomeric adhesive, FM1000 (Cytec Engineering Materials, MD, USA), was used to attach the sprayed substrate surface to a counter sample. Upon separation of the glued samples, two surfaces are generated. The counter sample holds de-bonded particles displaying the contact interface characteristics and the substrate specimen provides information about residual bonds. Together, these surfaces provide a complete image of the achieved particle/substrate bonding. Scanning electron microscopy (SEM, Oxford Instrument, EVO-MA10, Zeiss, UK), backscattered detector (BSD) and Energy-dispersive x-ray spectroscopy (EDS) have been used to study all specimens. An optical microscope (VHX-2000 Keyence, ON, CA) has been utilized to provide both top view images and 3D particle profiles.

**Table 3** CFD results of particle in-flight velocity and temperature (average and critical) for all three sets of powder taken from (Ref 31)

Particle velocity, m/s and temperature, °C	40 μm	58 μm	68 μm
<b>LPIT</b>			
Average	651 m/s, 51 °C	609 m/s, 36 °C	587 m/s, 34 °C
Critical ( $V_{C\_LPIT}$ , $T_L$ )	637 m/s, 40 °C	604 m/s, 35 °C	582 m/s, 33 °C
<b>HPIT</b>			
Average	626 m/s, 123 °C	586 m/s, 92 °C	574 m/s, 85 °C
Critical ( $V_{C\_HPIT}$ , $T_H$ )	593 m/s, 191 °C	568 m/s, 123 °C	561 m/s, 122 °C

The  $V_{C\_LPIT}$  and  $V_{C\_HPIT}$  relate to the critical velocity of LPIT and HPIT sprays, respectively. TL and TH refer to the LPIT and HPIT sprays particle temperature, respectively, traveling at these respective critical velocities

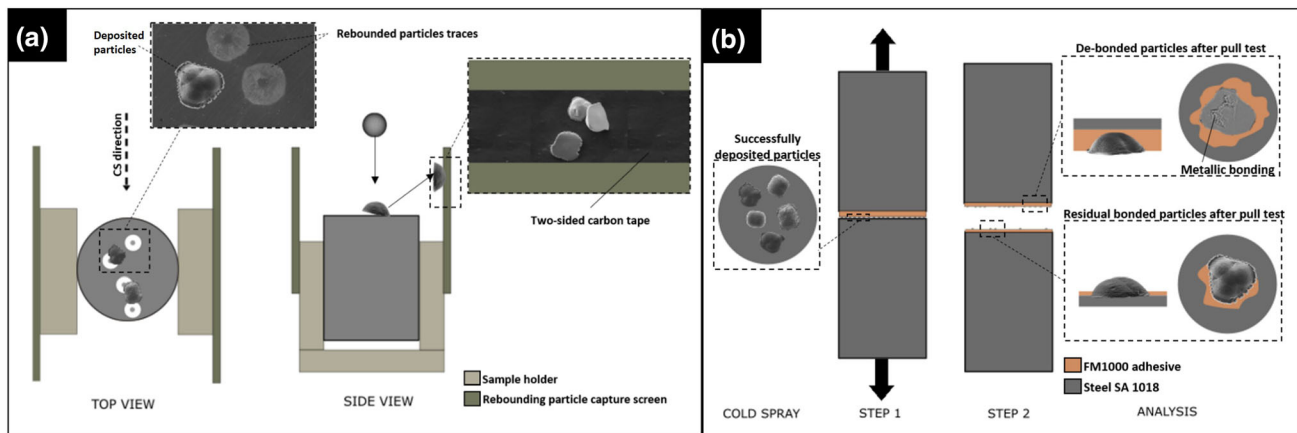


**Fig. 2** (a) Controlled scarce particle deposition and ensuing substrate surface analysis. Collection of rebounded particles process is illustrated through the side view of the spray set-up. (b) Single particle pull-test set-up providing information about the substrate and adhered particle state

## Finite Element Modeling

### Impact Process

The commercially available ABAQUS/Explicit finite element analysis (FEA) software has been used to study the effect of particle impact temperature on particle/substrate impact dynamics. The impact was simulated using a Lagrangian approach with quadrilateral coupled temperature–displacement elements (CAX4RT) for the aluminum particles and steel substrate, to properly capture the effect of heating due to plastic deformation. Figure 3 shows a schematic representation of the two-dimensional (2D) axisymmetric model. The mesh size was set to  $1/145 d_p$ , to ensure mesh independent results and proper resolution at the contact interface elements (Ref 11, 38). A fixed boundary condition was set on the substrate bottom surface. To eliminate the effect of reflective waves from substrate boundaries on the impact process and to avoid excessive computational costs, the substrate diameter ( $d_s$ ) and height ( $h$ ) were set to 10 times the particle diameter. The substrate was set at room temperature, 25 °C, for all cases.

The contact interaction at the particle/substrate interface is modeled using the surface-to-surface kinematic constraint enforcement method, which minimizes the penetration of contacting surfaces elements and consequently increases results accuracy. The interaction properties at the contacting surfaces have been described using a tangential penalty with a coefficient of kinetic friction,  $\mu_k$ , equal to 0.5 (Ref 8), a hard pressure-overclosure normal behavior and a heat generation formulation. The simulation total time was set to 100 ns to capture the full particle deformation and the beginning of rebound process from the substrate surface.

For a given powder size, the modeled particle impact velocity was kept constant between both HPIT and LPIT simulations to study solely the effect of impact temperature. For this purpose, a velocity of 637 m/s, 604 m/s and 582 m/s was chosen for powder set 1, set 2 and set 3, respectively. The particle impact temperatures found at the chosen velocities in both LPIT and HPIT sprays in (Ref 31) have been set as the initial particle temperature in the simulations. Consequently, temperatures of 40 °C, 35 °C and 33 °C in LPIT and 126, 93 and 87 °C in HPIT sprays

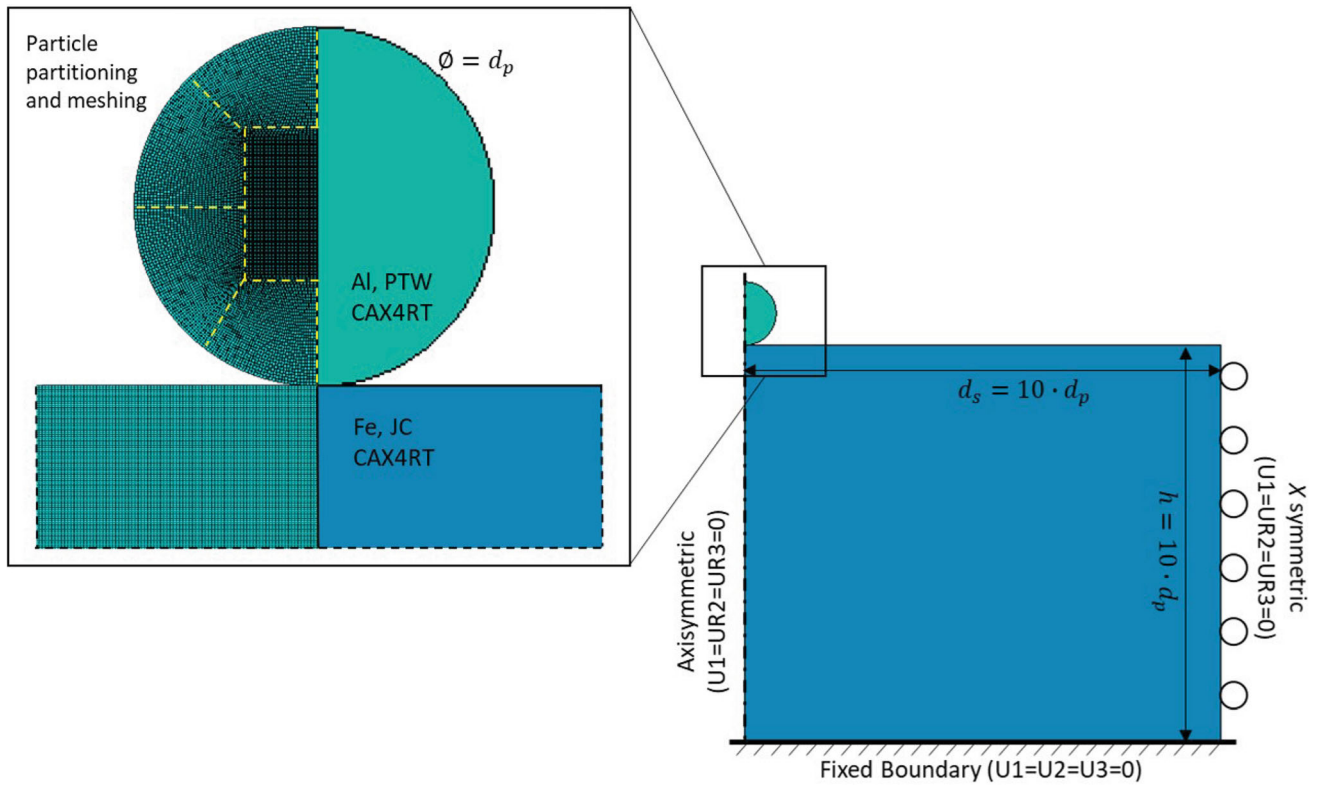


**Fig. 3** Initial configuration, boundary conditions and meshing technique of the axisymmetric numerical model

for powder set 1, set 2 and set 3, respectively, have been used.

**Material Properties**

The particle and substrate elastic response is modeled using the Mie–Grüneisen equation of state (EOS) through the linear  $U_s$ - $U_p$  Hugoniot relation to express the hydrodynamic stress, while a linear elastic model was utilized to express the deviatoric stress (Ref 8). The plastic response of the particle has been described using the Preston–Tonks–Wallace (PTW) model developed for high strain rate applications (Ref 39). The flow stress,  $\tau$ , is calculated using:

$$\hat{\tau} = \frac{\tau}{G_p(T)} = \frac{\sigma}{2G_p(T)} = 2 \left[ \hat{\tau}_s + \alpha \ln \left[ 1 - \varphi \left( -\delta - \frac{\theta \varepsilon_p}{\alpha \varphi} \right) \right] \right], \tag{Eq 3}$$

where

$$\alpha = \frac{s_0 - \hat{\tau}_y}{p}, \tag{Eq 4}$$

$$\delta = \frac{\hat{\tau}_s - \hat{\tau}_y}{\alpha}, \tag{Eq 5}$$

and

$$\varphi = \exp(\delta) - 1. \tag{Eq 6}$$

The  $\hat{\tau}_s$  and  $\hat{\tau}_y$  in the previous equations are the normalized work-hardening saturation stress and yield stress, respectively,  $\theta$  is the strain hardening rate,  $\varepsilon_p$  is the equivalent plastic strain,  $s_0$  is the saturation stress at 0 K,  $p$  is the strain hardening constant,  $\sigma$  is the Von Mises equivalent deviatoric stress and  $G_p$  is the plastic shear modulus. For simplicity, the shear modulus has been described as solely function of temperature, as previously shown to accurately describe the CGDS impacts (Ref 39);

$$G_p(T) = G_0 - \frac{D}{\exp\left(\frac{T_0}{T}\right) - 1}. \tag{Eq 7}$$

In the previous equation,  $G_0$  is the shear modulus at 0 K,  $D$  is a material constant,  $T_0$  is a temperature material constant and  $T$  is the material temperature. The PTW model is a modified version of the Voce law such that the work hardening is described as:

$$\frac{d\hat{\tau}}{d\varepsilon} = G_p(T) \frac{\exp\left[p \frac{\hat{\tau}_s - \hat{\tau}}{s_0 - \hat{\tau}_y}\right] - 1}{\exp\left[p \frac{\hat{\tau}_s - \hat{\tau}_y}{s_0 - \hat{\tau}_y}\right] - 1}. \tag{Eq 8}$$

At low strain rates, the plastic deformation process is governed by thermal activation, while at high strain rates, the plastic flow is controlled by dislocation drag

mechanisms. The maximum (high strain rate) and minimum (low strain rate) of the work-hardening saturation stress ( $\hat{\tau}_s$ ) and yield stress ( $\hat{\tau}_y$ ) are defined as:

$$\hat{\tau}_s = \max \left\{ s_0 - (s_0 - s_\infty) \operatorname{erf} \left[ \kappa \hat{T} \ln \left( \frac{\gamma \dot{\xi}}{\dot{\epsilon}_p} \right) \right], s_0 \left( \frac{\dot{\epsilon}_p}{\gamma \dot{\xi}} \right)^\beta \right\} \tag{Eq 9}$$

and

$$\hat{\tau}_y = \max \left\{ y_0 - (y_0 - y_\infty) \operatorname{erf} \left[ \kappa \hat{T} \ln \left( \frac{\gamma \dot{\xi}}{\dot{\epsilon}_p} \right) \right], \min \left\{ y_1 \left( \frac{\dot{\epsilon}_p}{\gamma \dot{\xi}} \right)^{y_2}, s_0 \left( \frac{\dot{\epsilon}_p}{\gamma \dot{\xi}} \right)^\beta \right\} \right\}, \tag{Eq 10}$$

where  $\hat{T} = T/T_m$ ,  $T_m$  is the melting temperature,  $s_\infty$  and  $y_\infty$  are the saturation and yield stress close to melting temperature, respectively,  $\kappa$  is the temperature dependence constant,  $\gamma$  is the strain rate dependence constant,  $\dot{\epsilon}_p$  is the plastic strain rate,  $\beta$  is the high strain rate exponent,  $y_0$  is the yield stress at 0 K,  $y_1$  is the medium strain rate constant and  $y_2$  is the medium strain rate exponent. The  $\dot{\xi}$  term in the previous equation is defined as:

$$\dot{\xi}(\rho, T) = \frac{1}{2} \left( \frac{4\pi\rho}{3M} \right)^{1/3} \left( \frac{G_p(T)}{\rho} \right)^{1/2}, \tag{Eq 11}$$

where  $M$  is the atomic mass and  $\rho$  is the density. It can be seen from inspection of Eq 9 and 10 that the error function and the influence of  $T_m$  dominate at low strain rates. The yield strength is dominated by strain rate when the strain rate value reaches a critical constant evaluated to be between  $10^5 \text{ s}^{-1}$  and  $10^8 \text{ s}^{-1}$  for aluminum (Ref 40). To complete the discussion on the plasticity model, the definition of the temperature change over time is also described:

$$\dot{T} = -\Gamma T \frac{\dot{v}}{v} + \frac{\sigma_{ij} \dot{\epsilon}_{ij}^p}{\rho C_v}, \tag{Eq 12}$$

where  $\Gamma$  is the Grüneisen gamma,  $v$  is the volume,  $\sigma_{ij}$  is the Cauchy stress tensor,  $\dot{\epsilon}_{ij}^p$  is the strain tensor and  $C_v$  is the specific heat with fixed volume. The first term in Eq 12 corresponds to the temperature rise (or drop) due to volume variations and the second term refers to the heating from plastic work. The temperature does not affect the integration of Eq 8 as it is uncoupled with the included integration variables, such as strain rate and strain. In addition, as the melting temperature is only used to normalize (scale) the temperature in the calculation of low strain rate work hardening saturation stress and yield stress, the effect of the melting temperature value is greatly diminished in high strain rate deformation, such as in those experienced in CGDS impact. If the local temperature in the model exceeds the material melting temperature, the material at this location will keep its hardening memory. This

assumption accounts for the latent heat thermal energy storage required to carry out the transformation from solid to liquid and prohibits the stress to drop to zero immediately as melting temperature is reached.

The substrate plastic deformation processes have been described using the Johnson–Cook (JC) model due to the lack of material properties available for the PTW formulation. The detailed theory, deformation model description of the elastic and plastic response and the material properties of both the aluminum and steel can be found in (Ref 8).

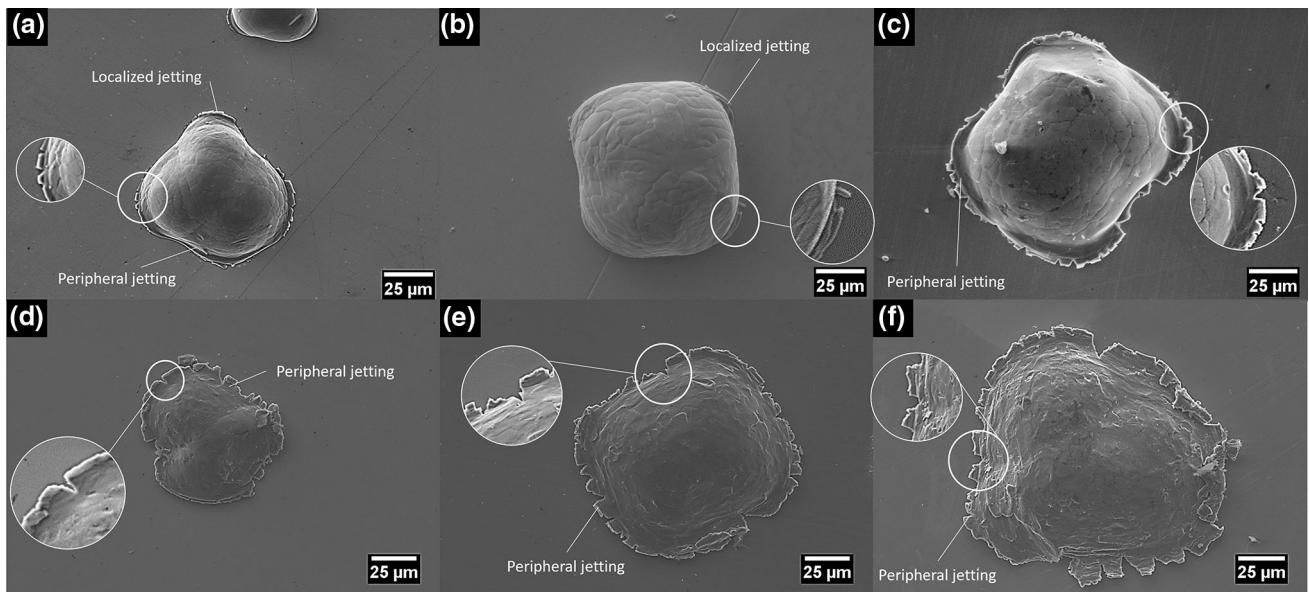
It has been shown that the alumina native oxide layer has an amorphous or semi-crystalline structure (Ref 36). However, lack of data pertaining to the amorphous or semi-crystalline oxide layer behavior under shock loading and the vast range of reported mechanical properties (Ref 41), dependent on alumina density, prohibits an exact description of the material properties. Hence, the native layer was not modeled and experimental interfacial material features, in particular grain deformation, have been used instead to assert the oxide presence or its proper removal.

## Results and Discussion

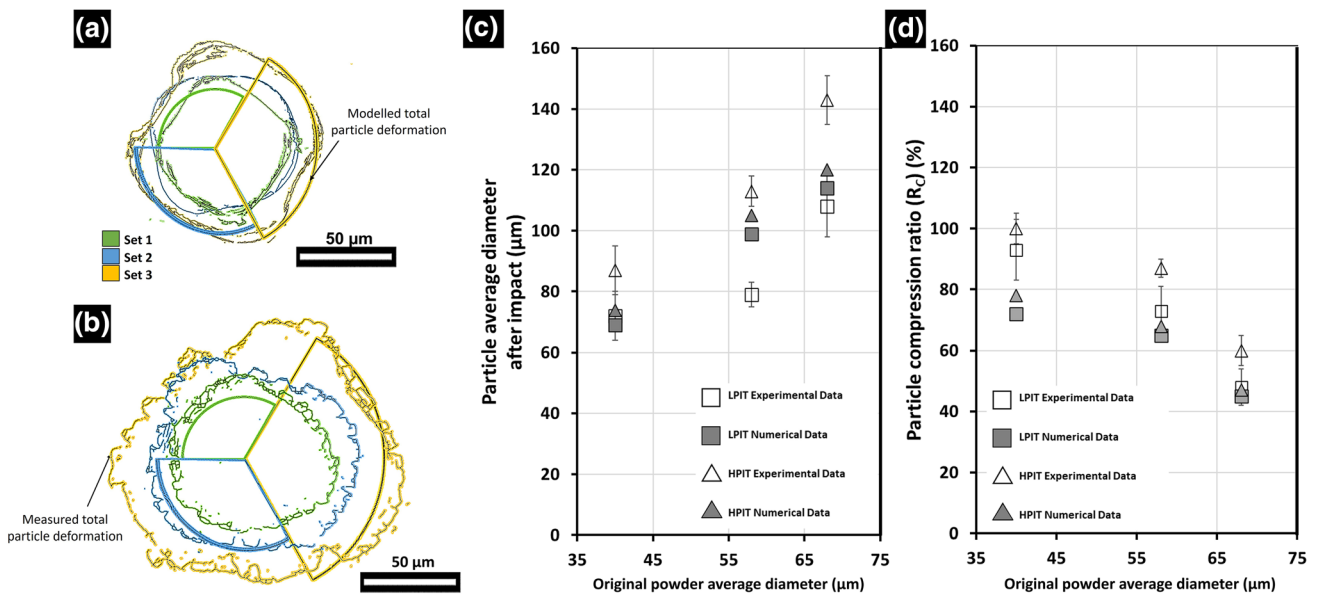
### Particle Deformation

Figure 4 shows the top view surface morphology of particles after deposition onto the steel substrate. Jetting features are observed for all cases. Particle outer edge cracking is observed for all cases, as highlighted in the inserts of Fig. 4. The jetting is more pronounced for HPIT due to the enhanced particle softening associated with the increased particle impact temperature, allowing greater material flow for the same stress field at the contact interface (Ref 27, 42, 43). The hard steel substrate undergoes no visible deformation near the particle periphery for all depositions from these top view images.

The particles deformation contours, as predicted by the model, are shown in Fig. 5(a) and (b) for LPIT and HPIT, respectively. Also shown, for each powder set, is a representative experimental particle outline as observed after impact on the substrate. Only a quadrant of the simulated particles is shown for each case, as the model is symmetrical, allowing better comparison with experimental results. A different color is used to distinguish each powder size set. Since constitutive phenomenological models are developed by fitting coefficients to visual inspection without any additional comparison to microstructural details, such as dislocation behavior and activity (Ref 39), they inherently fail at capturing details, such as the asymmetrical particle deformation observed in Figure 4, irrespective of the model dimensional space, i.e., 2D versus



**Fig. 4** Single particle deposition under LPIT (a, b, c.) and HPIT (d, e, f) conditions. Localized peripheral aluminum particle material jetting is identified. Particle jetting and edge cracking are magnified. Particle size prior to impact increases from left to right, i.e., from set 1 to set 3



**Fig. 5** Predicted deformation of particles after impact for (a) LPIT and (b) HPIT. A single representative outline of deposited particle contours measured by microscopy is provided for each powder set along with the corresponding numerical model prediction.

3D. Nevertheless, the PTW model successfully predicts the influence of particle size and temperature on final diameter size. Figure 5(c) compares the measured particle average diameter after impact and the corresponding predicted deformation/diameter for both LPIT and HPIT sprays for a given particle size. For a given powder size, the particle final diameter, i.e., contact area, increases with particle impact temperature.

Experimental and numerical data of (c) particle average deformed diameter and (d)  $R_C$  based on particle size and impact temperature are provided

Additionally, the particle compression ratio ( $R_C$ ), defined by

$$R_C = \frac{d_p - h_p}{d_p} \times 100\% \quad (\text{Eq 13})$$

has been calculated for each set, where  $d_p$  is the original average particle diameter for each set and  $h_p$  is the height of the flattened particle in the impact direction. Due to the expected limited hard steel substrate surface deformation,



the value of  $h_p$  has been estimated as the distance from the substrate to the particle top surface. The experimental and predicted  $R_C$ 's values are shown in Fig 5(d). For a given particle size, both results show an increase in  $R_C$ , i.e., flattening, with increasing particle impact temperature, i.e., increasing softening and plastic flow. The  $R_C$  decrease with particle size, easily observed for LPIT conditions, is solely attributed to the decrease in particle velocity rather than to the variation in particle diameter (Ref 38). Discrepancies between numerical and experimental values, presented in Fig. 5(c) and (d), stem from the lack of validated adequate PTW data for aluminum material under high strain rate deformation, as reported in the field (Ref 11, 40).

As observed from Fig. 4, the deposited particles shape is not spherical anymore, although particle sphericity is expected for symmetrical polycrystalline particle impacts, as commonly reported to be the case in CGDS (Ref 25, 44). Three specific types of particle shapes after impact have been detected, i.e., type 1: triangular, type 2: rectangular and type 3: square, and are shown in Fig. 6.

Since these precise shapes have been detected for all three powder size sets, under both high and low impact temperature conditions, it is suggested that their occurrence is related to particle microstructure, i.e., crystallographic texture, rather than impact characteristics (size, temperature, and velocity). Particle's microstructure influence on its final shape upon high-speed impact has been described in molecular dynamics (MD) studies. Similar powder shapes to the ones reported in the current work have been observed recently in MD impact studies for single crystal copper particles (Ref 45). The final particle shapes in the MD work have been associated with the initial particle crystal orientation with respect to the impact loading direction (Ref 45). Since the current study also deals with an FCC material, for which the slip systems are defined along  $\{111\}$  planes and  $\langle 110 \rangle$  directions, the conclusions related to the particle crystal orientation influence on sliding directions, slip system activation and stacking faults formation obtained using MD are deemed relevant. The

triangular particle shape, as shown in Fig. 6(a), has been proven to result from an initial  $[111]$  crystal orientation. The rectangular and square shapes have been associated with single crystal particles oriented in the  $[110]$  and  $[100]$  directions, respectively. Hence, the current particle material behavior suggests presence of preferential grain orientation with narrow distribution and/or important fraction of low angle grain boundaries and/or critical grain alignment/geometry.

In the current study, due to the constrained substrate deformation, i.e., limited geometrical restrictions, it is believed that the particle shapes result solely from particle microstructural characteristics. This anisotropic particle behavior affects both the particle final deformation and  $R_C$ , i.e.,  $[100]$  orientation allowing the greatest and  $[110]$  the lowest compression (Ref 45), which can also explain the standard deviations and divergent experimental and numerical results shown in Fig. 5.

### Substrate Contact Traces

As shown by the substrate surface images in Fig. 7, circular traces are left on the steel substrate surface after the impact of unsuccessfully adhered (rebounded) particles. The circular traces have been analyzed using EDS; however, the quantity of the remnant or removed material in these regions was insufficient to confirm their nature. The traces are spherical irrespective of particle size, impact characteristics and particle final shape. The LPIT traces show no remnant aluminum material, while evidence of local residual aluminum is observed on all HPIT traces, as indicated by the yellow arrows in Fig. 7(j), (k) and (l). These remnants are mostly detected at the trace periphery and their occurrence decreases as particle size increases. Since particles within the same powder set impact the substrate at similar velocities but at different temperatures, it is suggested that the impact temperature affects the traces characteristics. Remnant material alludes to the presence of high pressure and surface expansion at the trace periphery

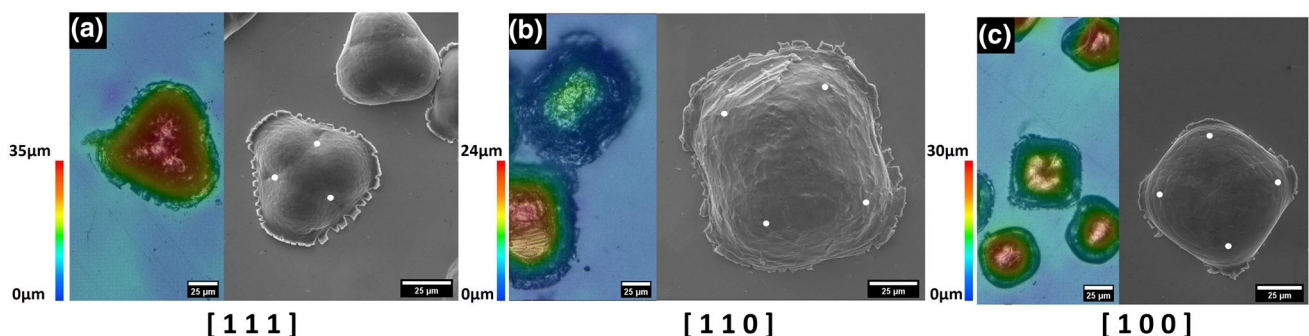


**Fig. 6** Deposited particles top view displaying all three detected final shapes; (a) triangular, (b) rectangular and (c) square. Particle 3D height profile with corresponding scale along with SEM images are provided for all three shapes

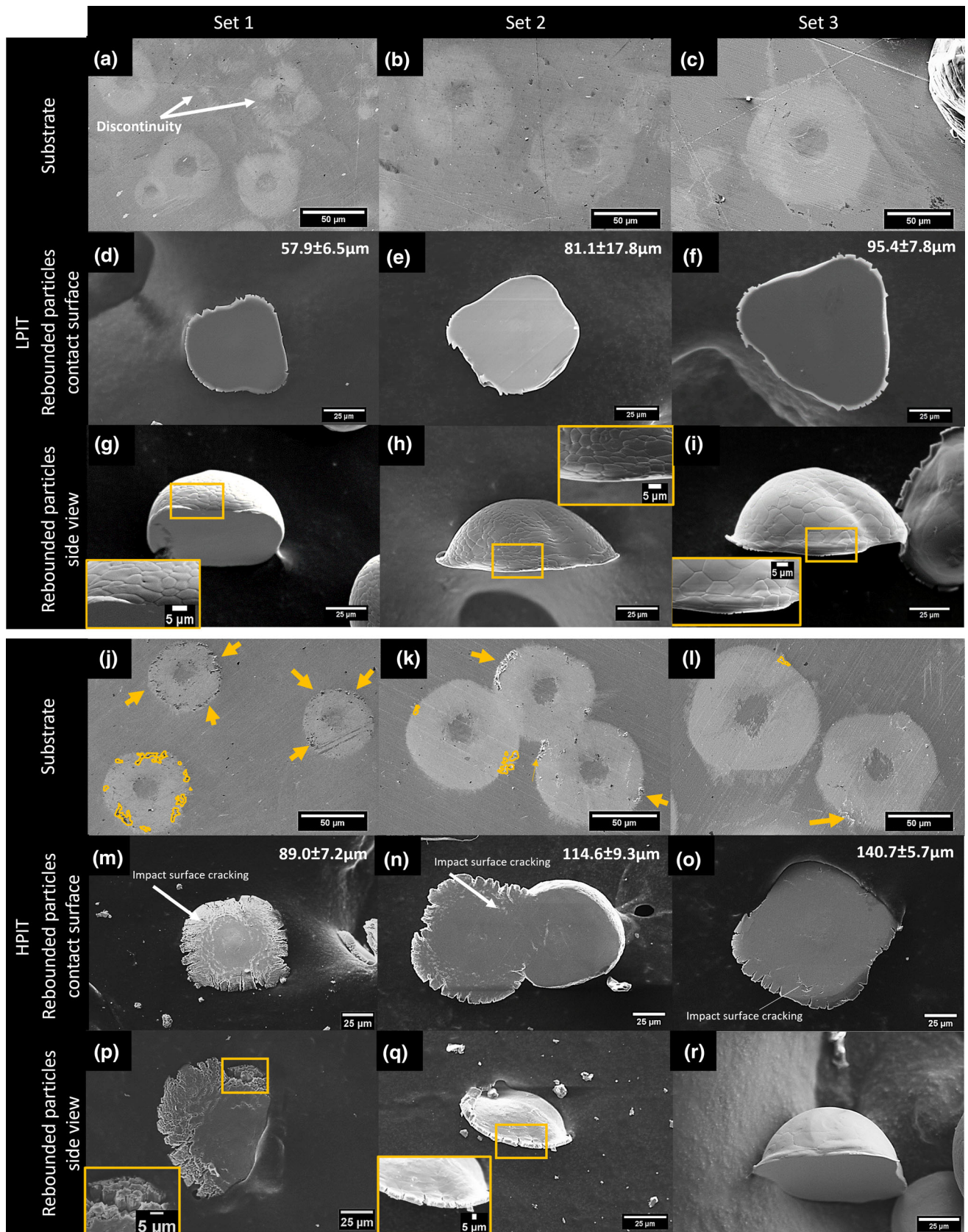


**Fig. 7** Traces on steel substrates left by rebounded particles for both LPIT (a, b and c) and HPIT (j, k and l) impacts and for all three size sets. Remnant aluminum material on the steel substrate surface is highlighted in yellow. LPIT discontinuous traces are indicated by white arrows. The rebounded particle impacted surface for LPIT (d, e and f) and HPIT (m, n and o) are shown along with their corresponding average diameter. Side views of the collected rebounded particles, showing grain deformation at the jetting zone, are given for both LPIT (g, h and i) and HPIT (p, q and r)

(Ref 46). Since the compressive contact pressure, surface expansion and temperature are lowest at the particle jetting edge, the traces are considered to originate from interfacial phenomena rather than from particle total deformation.

Figure 7 also includes samples of the collected rebounded particles for each powder set (contact surface and side view). The average diameter of the collected particles, provided in Fig. 7, is very close to the deposited particles diameter, shown in Fig. 5, implying that their impact characteristics (velocity and temperature) are not far from critical values. Jetting-like features are observed at the rebounded particles periphery for all cases, increasing with particle temperature increase (HPIT vs. LPIT), which confirms that jetting does not necessarily correlate with successful bonding (Ref 47-49). For LPIT, the collected particles present a clean interfacial surface with no signs of cup-and-cone, protruding material or any other visible features related to metallurgical bonding detectable through SEM. For HPIT, the impacted particle surface shows signs of micro-cracking, which increases as the particle size decreases. The micro-cracking can be associated with the presence of large tensile stresses related to the intensive surface expansion and/or to the presence of rapid interfacial heating and cooling processes.

The numerical model has been used to try to identify the interfacial characteristic causing the ring traces appearance on the substrate surface. Figure 8 highlights the particle contact surface area experiencing temperatures above the aluminum melting point for LPIT powder set 3. However, as the constitutive finite element models do not account for material phase transitions, i.e., melting, results above material melting point should be analyzed with proper caution and interpreted as potentially still being at melting point. In most models involving plastic deformation, the melting temperature is assumed to be constant (Ref 39, 40, 50, 51). However, in high strain-rate impacts involving large pressure variations, the melting temperature increases drastically with pressure. The melting curve of aluminum indicates that at 4 GPa the aluminum melting temperature reaches 927 °C (Ref 52). A linear trendline has been curve fitted to published results (Ref 52) to extract the relation between pressure and melting temperature up to pressures recorded in the current CGDS impact, i.e., < 4

GPa. Subsequently, the ratio  $\varphi$  has been utilized to determine the particle interfacial regions that reach melting temperatures given the instantaneous contact pressure they experience:

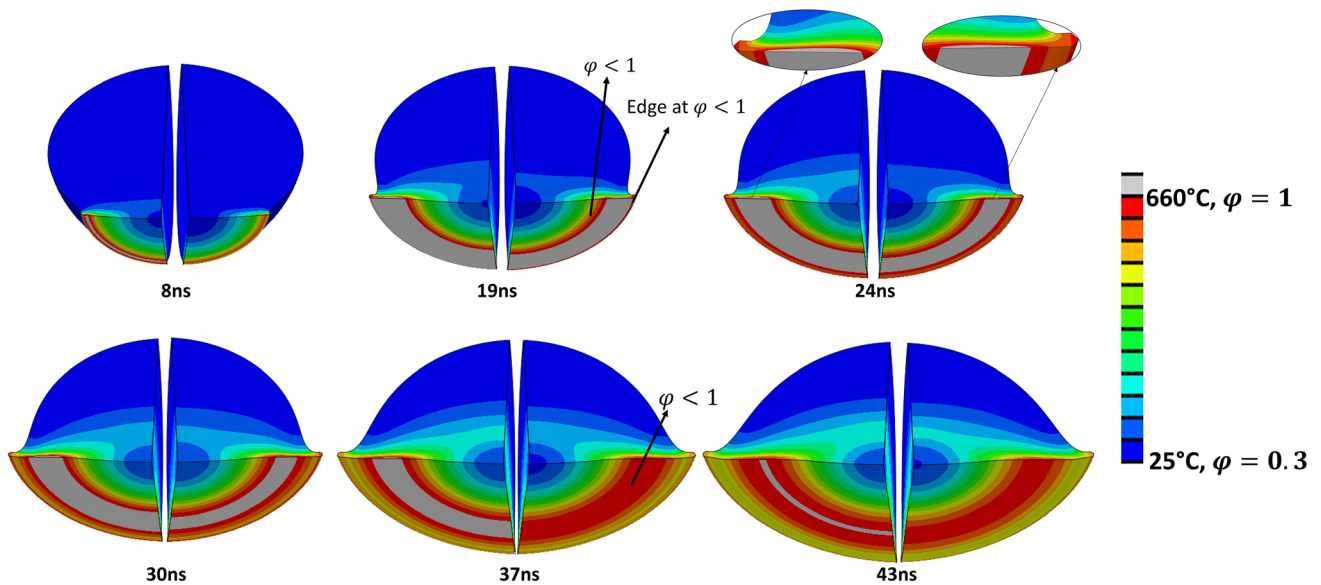
$$\varphi = T/T_{m,p}, \quad \begin{cases} \varphi < 1, & \text{below melting} \\ \varphi = 1 & \text{at melting} \\ \varphi > 1 & \text{high - temperature melting} \end{cases} \quad (\text{Eq 14})$$

where  $T$  is the existing current element temperature and  $T_{m,p}$  is the temperature required to generate melting at the exposed pressure. Figure 8 shows the effect of contact pressure on the melting temperature at the LPIT powder set 3 interface.

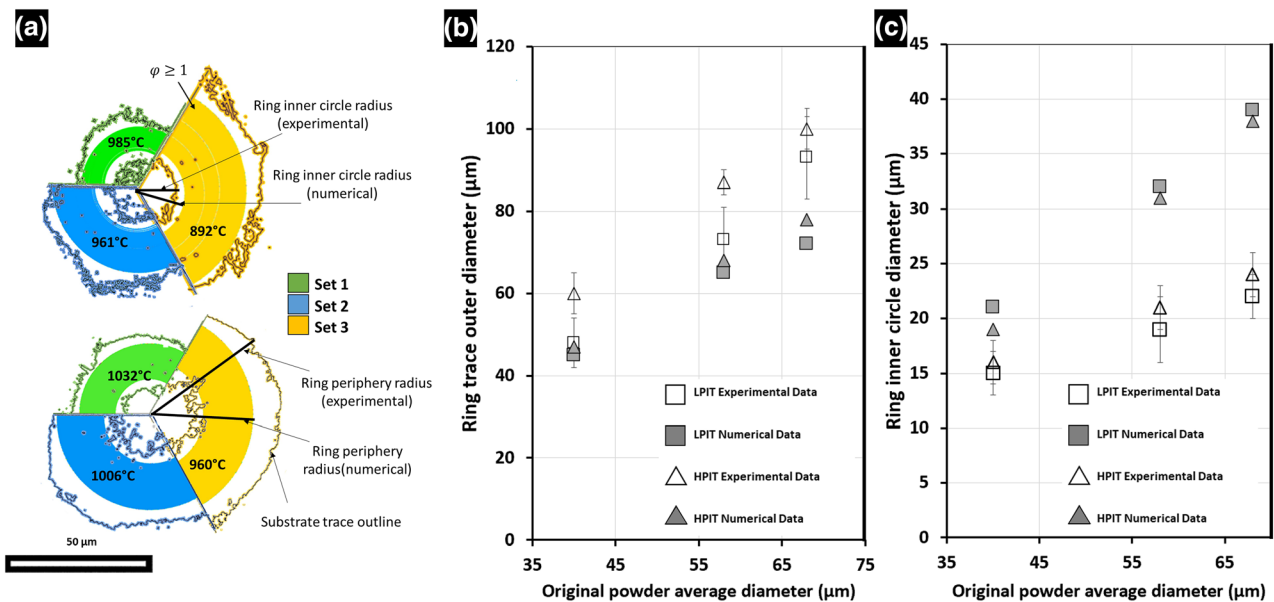
A value of  $\varphi$  of 1 is seen to persist up to 30 ns, while the pressure-independent melting temperature, i.e., 600 °C, holds up to 43ns. In addition to shortening the period under which melting temperature exists, the pressure also decreases the size and thickness of particle material experiencing melting temperatures.

Figure 9(a) illustrates the computed interfacial zones with  $\varphi = 1$  for all spray conditions. An experimental representative trace left by the impact is outlined for each case. The same color code as in Fig. 5 is used to discern results between powder sets. The zone with temperatures at/or above the aluminum melting point also appears in a ring-like shape, for which the ring trace outer diameter and ring inner circle diameter are also reported in Fig. 9(b) and (c), respectively, along with the experimental measurements. The periphery of these regions is seen to increase with particle diameter and impact temperature increase while the inner circle diameter sees only slight changes with varying particle impact characteristics, which resembles the experimental traces behavior.

The measured outer diameter increases from 48 μm (set 1) to 93 μm (set 3) for LPIT while these values rise from 60 μm (set 1) to 100 μm (set 3) for HPIT sprays. The rebounded particle diameter for each powder set and impact condition, shown in Fig. 7, is also far from these ring-shape trace dimensions, which once again confirms that the traces are related to specific interfacial phenomena rather than particle deformed size. The inner circle diameters increase by less than two microns with the increase in particle temperature for a given particle size. For LPIT, an increase in the ring inner circle diameter from 15 to 22 μm is recorded with the increase in particle diameter from powder set 1 to powder set 3. These values increase from 16 to 24 μm for HPIT deposition. The same trends are observed in the numerical model, as shown in Fig. 9, suggesting a link between the traces and particle high-temperature zones. Deviations from experimental traces dimensions and these zones can stem, once again, from the inaccuracy of the pure aluminum properties utilized in the



**Fig. 8** Particle temperature (particle left-side) and particle pressure-dependent melting temperature factor  $\phi$  (particle right-side) at the interface of LPIT powder set 3 impacts over time. Included inserts show the effect of pressure through particle thickness



**Fig. 9** (a) Illustrations showing a single representative substrate trace outline along with the corresponding numerical zone experiencing melting temperatures for LPIT (top) and HPIT (bottom) impacts.

(b) The trace outer periphery and (c) ring inner circle diameter measurements are compared with the numerical results of particle contact surface area experiencing temperatures above melting point

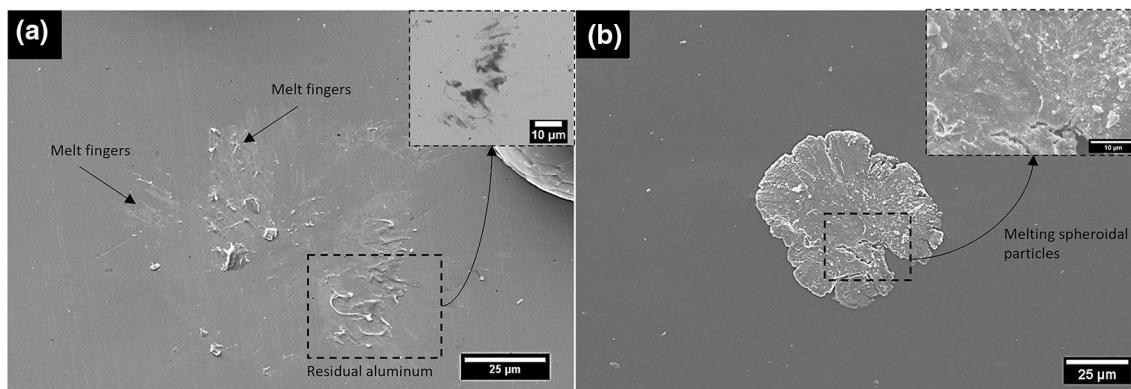
PTW model and its inability to predict the exact deformation and anisotropic particle behavior.

Figure 9(a) also shows the maximum temperature reached on the particle contact surface during its deformation. For LPIT, the maximum particle contact surface temperature decreases, from 985 to 892 °C, with decreasing particle impact velocity from 637 m/s (powder set 1) to 582 m/s (powder set 3). Increasing particle impact temperature, i.e., HPIT sprays, raises the temperature at the

particle contact surface. An increase of 47 °C and 68 °C is observed for powder set 1 and powder set 3, respectively when depositing from LPIT to HPIT conditions.

### Particle Melting

Material features associated with melting have been detected at the particle and substrate contact surfaces, as seen in Fig. 10. In the case of LPIT, small fingers radiating



**Fig. 10** SEM and BSD analysis of melt-related features. (a) Melt fingers observed on the substrate surface after rebound of a LPIT particle. (b) Spheroidal particles formed on the HPIT contact surface after rebounding

from the particle impact location are observed on the substrate surface, as shown in Fig. 10(a). The finger-shaped splashing has been vastly correlated to interfacial liquid film flow and its rapid solidification in thermally sprayed particles (Ref 53, 54). The radiating fingers leave traces of contact on the substrate surface similarly to the ones detected in Fig. 7, further reinforcing the association of high-temperature zones with the detected traces. The BSD insert in addition to an EDS analysis of the impacted area confirm that the remnant material consists solely of aluminum. For HPIT sprays, nano-sized spheroidal particles were formed on the surface of the rebounded particles, as shown in Fig. 10(b). These small ejecta particles have been associated with fast solidification of liquid material (Ref 2, 55).

Both the spheroidal particles and melt fingers validate the presence of melting temperatures, which is in good agreement with the model prediction shown in Fig. 9. Melting features have been more frequently observed for HPIT than for LPIT sprays since increasing impact temperature leads to improved plastic deformation, i.e., thermal softening, and consequently to superior frictional heating and localized temperature rise. Additionally, for LPIT sprays, melting characteristics have been predominantly observed in powder set 3.

Based on the model, the material found above the aluminum melting temperature reaches a thickness of 0.45  $\mu\text{m}$  for LPIT powder set 1 up to 0.50  $\mu\text{m}$  for powder set 3. These values are larger for HPIT impacts and reach 0.60  $\mu\text{m}$  and 0.70  $\mu\text{m}$  for powder set 1 and set 3, respectively. Although the occurrence of melting, restricted to this localized thin film interfacial layer in CGDS impact, has minor influence on the overall particle deformation, melting can have an important role in the particle bonding process. Observations from Fig. 10 demonstrate that the particle rebound energy is sufficient to overcome the particle adhesion.

Figure 11(a) shows the propagation of the interfacial zone found above melting temperatures and points to the location of potential melting. The rapidly cooling elements delineate the region that undergoes rapid cooling processes, as illustrated in Fig. 11(a). The strong compressive shock propagating inside the particle upon impact generates high temperatures in the particle material behind the shock front and elements reaching melting temperature are seen to cool down quickly during particle deformation. As the shock propagates and reflects on the particle boundaries, it leads to rapid interfacial heating and cooling processes in the first few nanoseconds of the impact, as illustrated in Fig. 11(a) for the HPIT powder set 3.

Experimental observations, shown in Fig. 11(b), confirm the existence of the rapidly cooling zone, as traces of melting are not observed on the substrate surface. Aside from rapidly cooled regions, an interfacial zone, referred to as stagnant zone, is comprised of elements which experience melting temperatures for enough time to eventually lead to melting, as shown to be the case for the impact observed in Fig. 11(b). In this stagnant zone, enough energy is absorbed at the same localized region to induce melting, i.e., above the aluminum latent heat of fusion. The outward spreading of the molten material, as observed in Fig. 11(b), stems from the particle simultaneous outward deformation. If the solidification process of the molten material is lengthier than the particle residence time on the substrate surface, the liquid melted interface hinders adhesion as it provides low mechanical particle/substrate interface strength (Ref 56), as seen to be the case for the impact of Fig. 11(b). For HPIT, this stagnant region persists for 18 ns and 26 ns for powder set 1 and set 3, respectively, while these values reach 11 ns and 18 ns for LPIT conditions, thus showing an increase with both impact temperature and particle size. Experimental observation along with the numerical melt propagation validates, once more, the nature of the substrate traces.

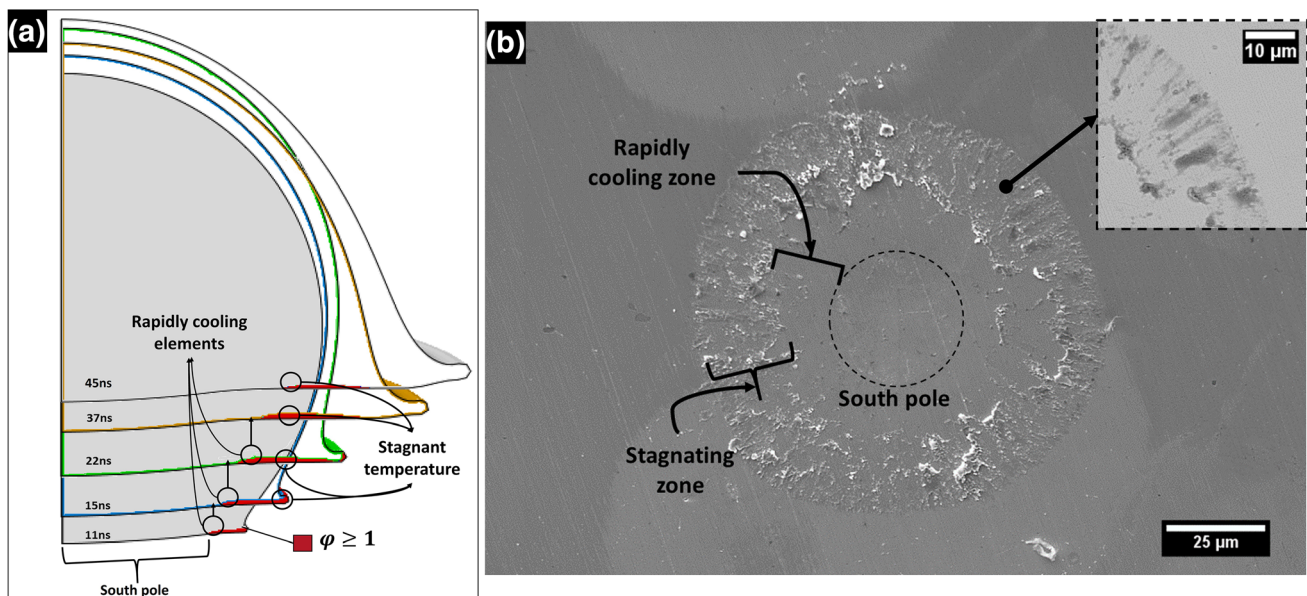


**Fig. 11** (a) Modeling results illustrating the melting temperature propagation process. Elements with  $\phi \geq 1$  are highlighted in red. Elements undergoing rapid cooling during particle deformation are highlighted. Elements experiencing melting temperatures for long periods of time are also emphasized (stagnating elements).

### Particle Bonding

The experimental observations indicate that jetting, micro-cracking and melting features are not necessarily associated with successful bonding. The interfacial features of removed adhered particles are now analyzed, and FEM contact characteristics are evaluated to identify the bonding requirements under LPIT and HPIT conditions. Table 4 presents the coating adhesion for each powder set and both LPIT and HPIT conditions, as reported in (Ref 31).

### Single Particle Debonding

Figure 12(a) displays the adhesive and particle surface that were in contact with the substrate after mechanically detaching the particles. A large quantity of particles, within each tested condition, did not show any signs of features related to metallic bonding, implying that the bonded regions were too small to be detected using SEM. Furthermore, some particles remained bonded to the substrate surface after pulling test, as a result of larger bond strength,

Experimental substrate surface observations (SE and BSD) after the impact and subsequent rebound of a HPIT powder set 3 show the existence of rapidly cooling elements, which leave no traces of aluminum, and of stagnating elements, which leave remnant particle material on the substrate

i.e., leaving a particle indent in the adhesive, as shown in Fig. 12(a). For LPIT, the number of particles that remained adhered to the substrate surface was low irrespective of powder size, as shown in Fig. 12(a) for powder set 3. For HPIT, the fraction of particles remaining bonded onto the substrate increased with particle size decrease, which suggests increasing bonding strength with particle decreasing size.

Pulled particles display a vast size range of metallic bonding signs within each deposited powder set and condition. Despite deposition under wipe test conditions, sequential deposition of incoming particles on a previously deposited particle and consecutive impacts followed by rebounding process have been detected, as shown in Fig. 12(b) to (e), which can affect the observed bonded zones. Figure 13 shows magnified single particle contact surfaces to emphasize on the detected bonded regions. As shown, for both HPIT and LPIT sprays, regions with signs of metallic bonding are not uniformly distributed on the contact surface. This can be associated with angular impact, irregular oxide removal of non-uniform oxide

**Table 4** Coating adhesion strength as reported in (Ref 31)

Coating properties	Powder set 1	Powder set 2	Powder set 3
LPIT, $\sigma_{\text{adhesion}}$ , (MPa)	$34.8 \pm 7.5$ MPa	$60.0 \pm 19.4$ MPa	$71.7 \pm 13.5$ MPa
HPIT, $\sigma_{\text{adhesion,cohesion}}$ , (MPa)	$> 71.2 \pm 13.4$ MPa*	$> 61.0 \pm 10.6$ MPa*	$32.3 \pm 10.8$ MPa**

\*Local coating failure, refer to (Ref 31)

\*\*Adhesion and cohesion failure

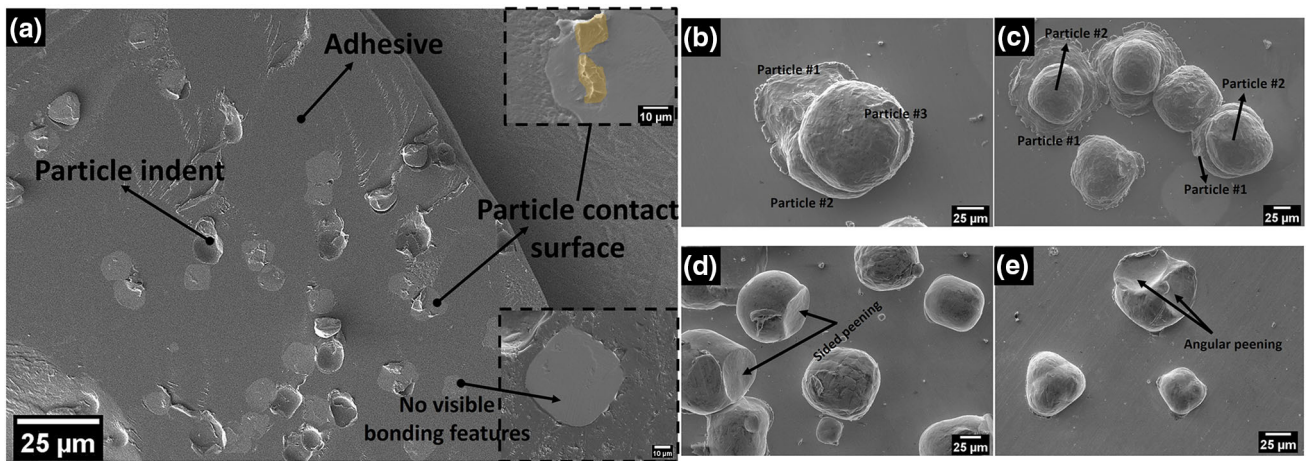


**Fig. 12** (a) Contact surface of pulled LPIT powder set 3 particles held within the utilized adhesive. Particles with and without bonding signs are highlighted in black boxes. Features related to metallic bonding are highlighted in yellow. Deposited particles during wipe

test showing presence of (b) successive skewed impact, (c) symmetrical consecutive impact, (d) angular impact of rebounding particles and (e) multiple angular impact of rebounding particles

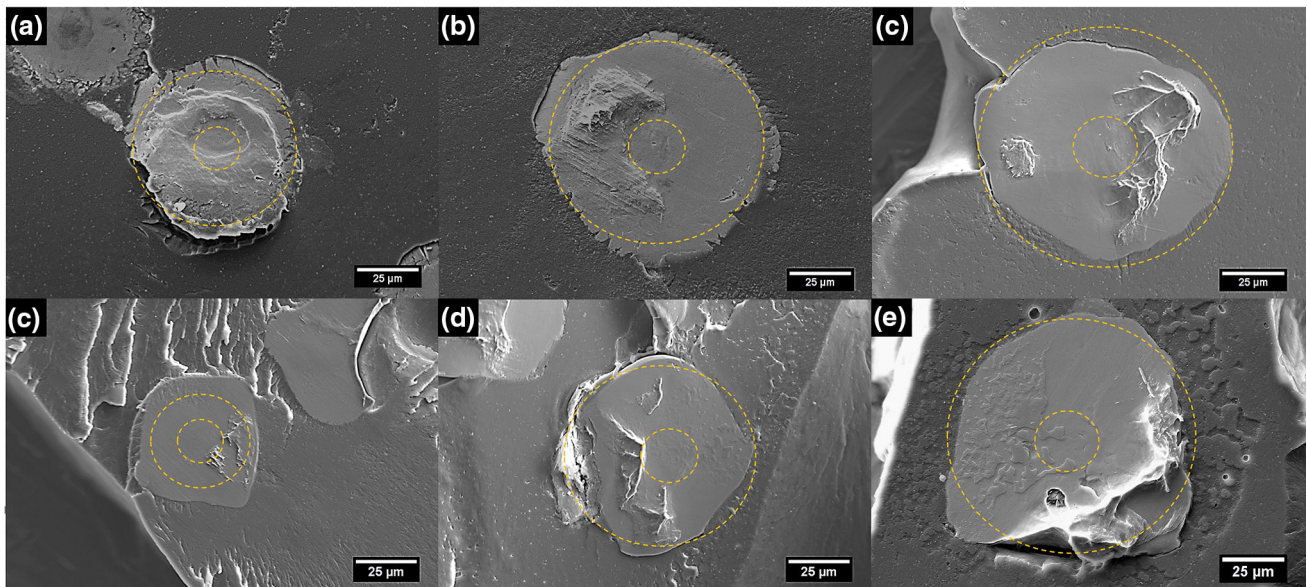


**Fig. 13** Particle impacted surface after removal from the substrate for all HPIT (top) and LPIT (bottom) sprays. Particles from powder set 1 (a–c), set 2 (b–d) and set 3 (c–e) are shown. The size of the measured traces on the substrate surface is delineated in yellow

thickness, distorted particle grain-dependent deformation and successive arbitrary impact (as shown in Fig. 12). Although different types of bonding features have been detected within all three sets of powders, the HPIT powder set 1 shows the highest zone of metallic bonding signs on the particle contact surface, as shown in Fig. 13(a).

In addition to lacking visible metallic bonding features as observed in Figs. 13, 14 shows that the particle south pole experiences limited deformation as the original powder grain morphology is still observed even after impact for both LPIT and HPIT conditions. This confirms the lack of adequate deformation and consequently limited potential

for native oxide removal at the south pole, preventing metallic bonding to occur in this region (Ref 48, 57–59).

### Particle Bonding Process

Bonding between two metal surfaces cannot occur until a surface expansion ratio threshold is reached (Ref 60). A larger  $R_c$ , suggests improved contact surface expansion (and enhanced oxide layer removal) and potentially larger bonding zones. This can explain the large adhesion strength of powder set 1 coating sprayed under HPIT conditions, as reported in Table 4. In addition, it has been shown that the

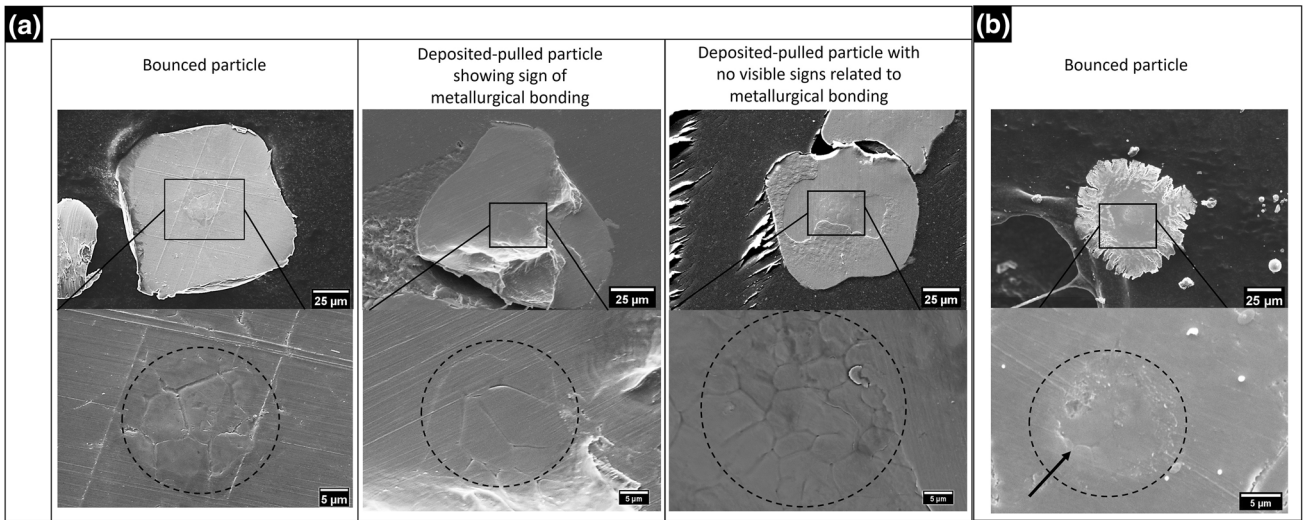


**Fig. 14** Experimental evidence of particle south pole limited deformation. Original powder grain morphology is detected in both (a) LPIT and (b) HPIT sprays

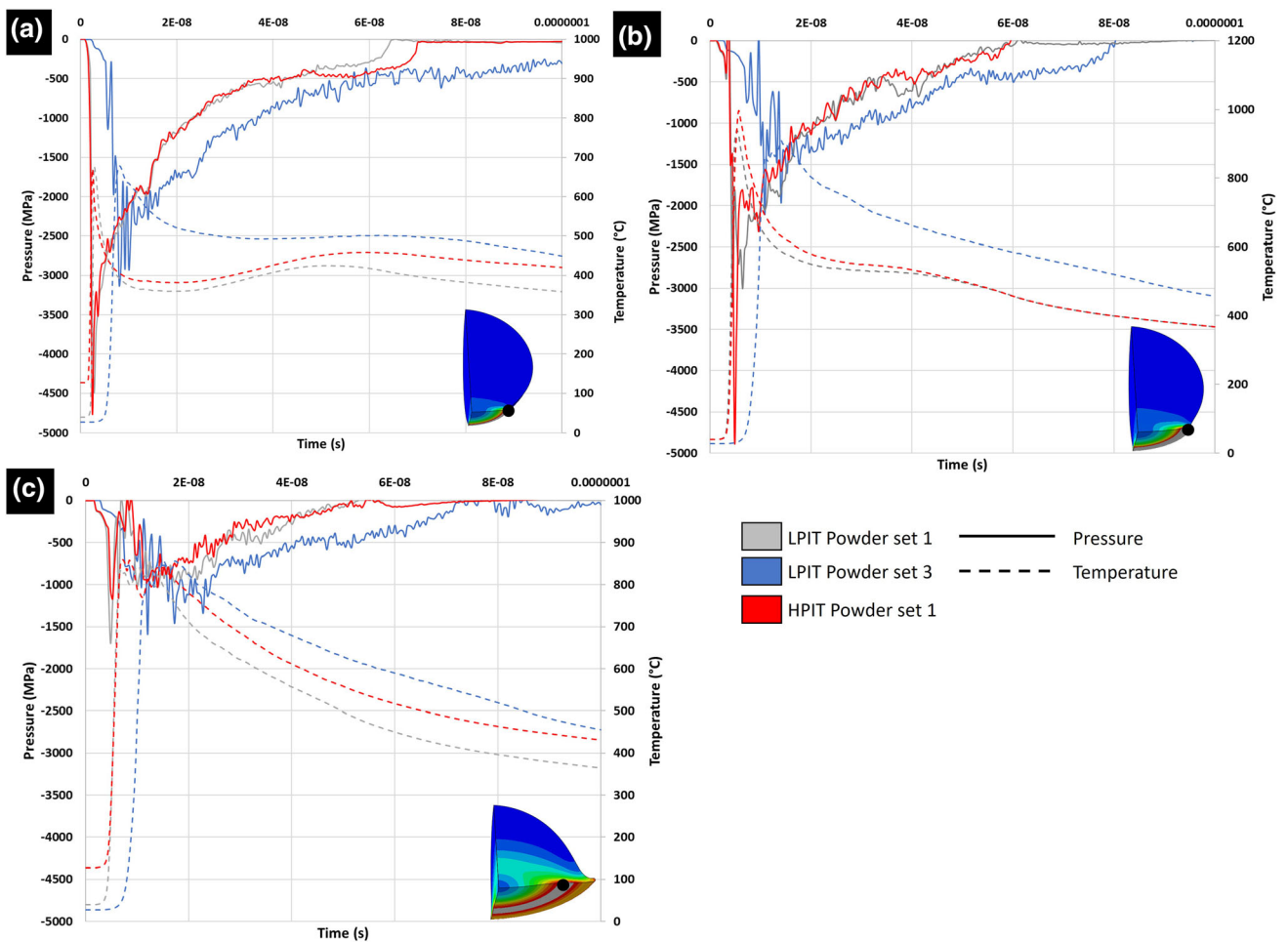


**Fig. 15** LPIT powder set 1 and set 3 and HPIT powder set 1 contact pressure and temperature temporal evolution at (a) the first element found above melting temperature, (b) for the element found at highest temperature and (c) for an element found in the stagnant region of the high-temperature propagation zones. Studied elements are identified using a dot in the provided inserts



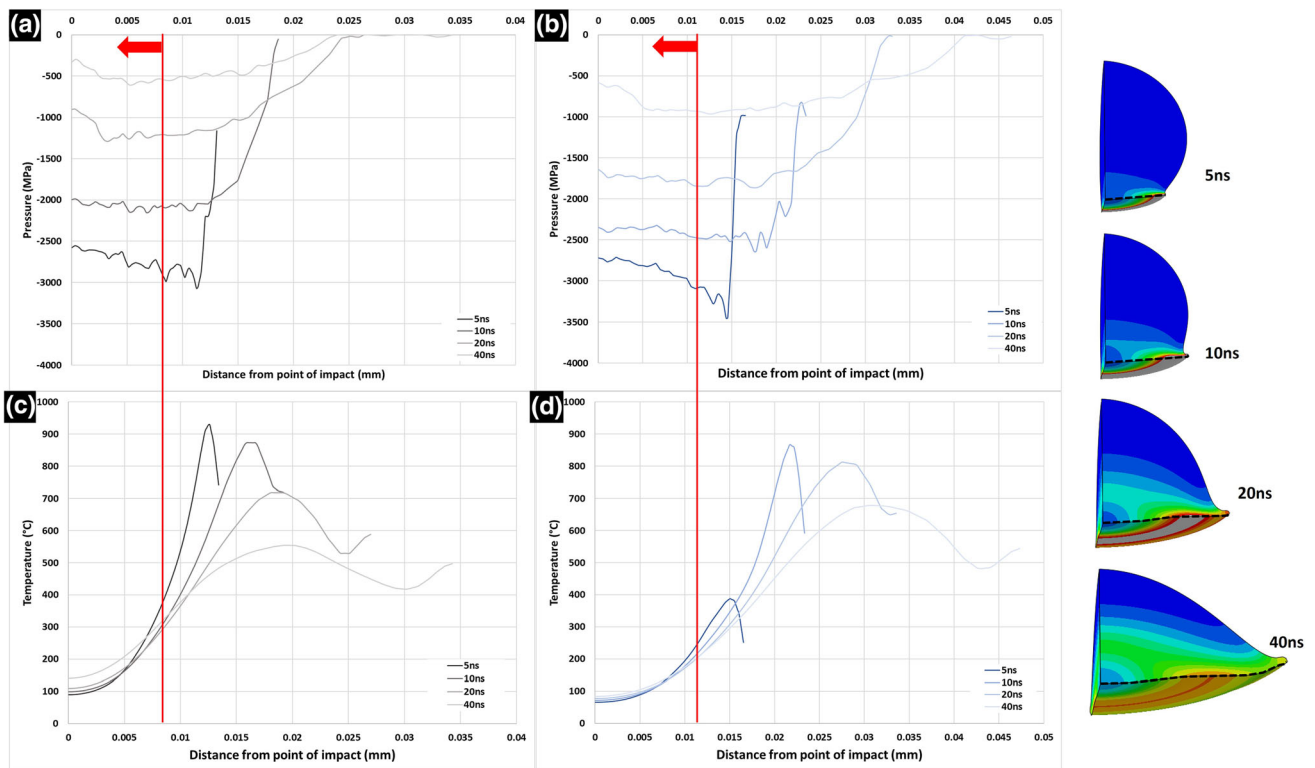


**Fig. 16** Particle contact surface characteristics at 5 ns, 10 ns, 20 ns and 40 ns after impact. Compression pressure for LPIT for (a) powder set 1 and (b) powder set 3. Temperature for LPIT (c) powder set 1 and

(d) powder set 3. The provided red line illustrates the particle contact surface radius lacking metallic bonding signs based on experimental observations/measurements

bond strength between two metal surfaces, deprived of native oxide layers, is function of the applied pressure, i.e.,  $\sigma_{adhesion} \cong \sigma_{22}$ , (Ref 60). The influence of particle velocity/size and impact temperature on the evolution of interfacial  $\sigma_{22}$  pressure is shown in Fig. 15 for three elements found at the particle contact surface of LPIT powder set 1 and set 3 and HPIT powder set 1. The first element corresponds to the location reaching first melting temperature, the second element experiences the highest temperature during deformation, and the third element is located in the region undergoing melting temperatures for the longest time period. All three elements are found in regions where bonding has been detected and within the area covered by the substrate traces. As shown in Fig. 15, increasing particle impact temperature has limited influence on the interfacial  $\sigma_{22}$  value while the  $\sigma_{22}$  peak value is seen to increase with particle velocity increase, i.e., size decrease in the current study.

Figure 15 also shows that although pressure and temperature peak values are largest for HPIT powder set 1,  $\sigma_{22}$  quickly drops to values lower than those recorded in LPIT powder set 3 after  $\sim 15$  ns. This indicates that the strong metallic bonding of HPIT powder set 1, supported by the large metallic bonded features observed in Fig. 13, high coating adhesion strength presented in Table 4 and largest

quantity of unsuccessfully removed particles, must have occurred within these first 15 ns. Additionally, it is within this time frame that melting temperatures appear, which emphasizes the importance of temperature in metallic bonding. The LPIT powder set 1, however, has displayed the lowest amount of metallic bonding features, as shown in Fig. 13, at the contact interface. Since both HPIT and LPIT powder set 1 impacts generate similar interfacial  $\sigma_{22}$  values, the low coating adhesion strength reported for LPIT powder set 1 can only stem from limited surface expansion and consequently improper oxide layer extrusion within the first 15 ns due to low impact temperature under which it deposits. Accordingly, the fraction of bonded particle area at the interface is seen to increase with temperature, as shown previously in Fig. 13, providing a larger particle/coating adhesion strength (Ref 61). Hence, the bonding process of LPIT powder set 1 is believed to occur only after the  $\sigma_{22}$  peak value, as shown in Fig. 15.

Despite not achieving the temperature and pressure peak values of powder set 1, particles from powder set 3 hold higher contact compressive pressure, due to larger kinetic energy, and temperature after 15 ns, as shown in Fig. 16. The powder set 3 also deforms under low  $R_c$ , as reported in Fig. 5(d), implying that proper surface expansion might not be reached quickly following impact. An increase in

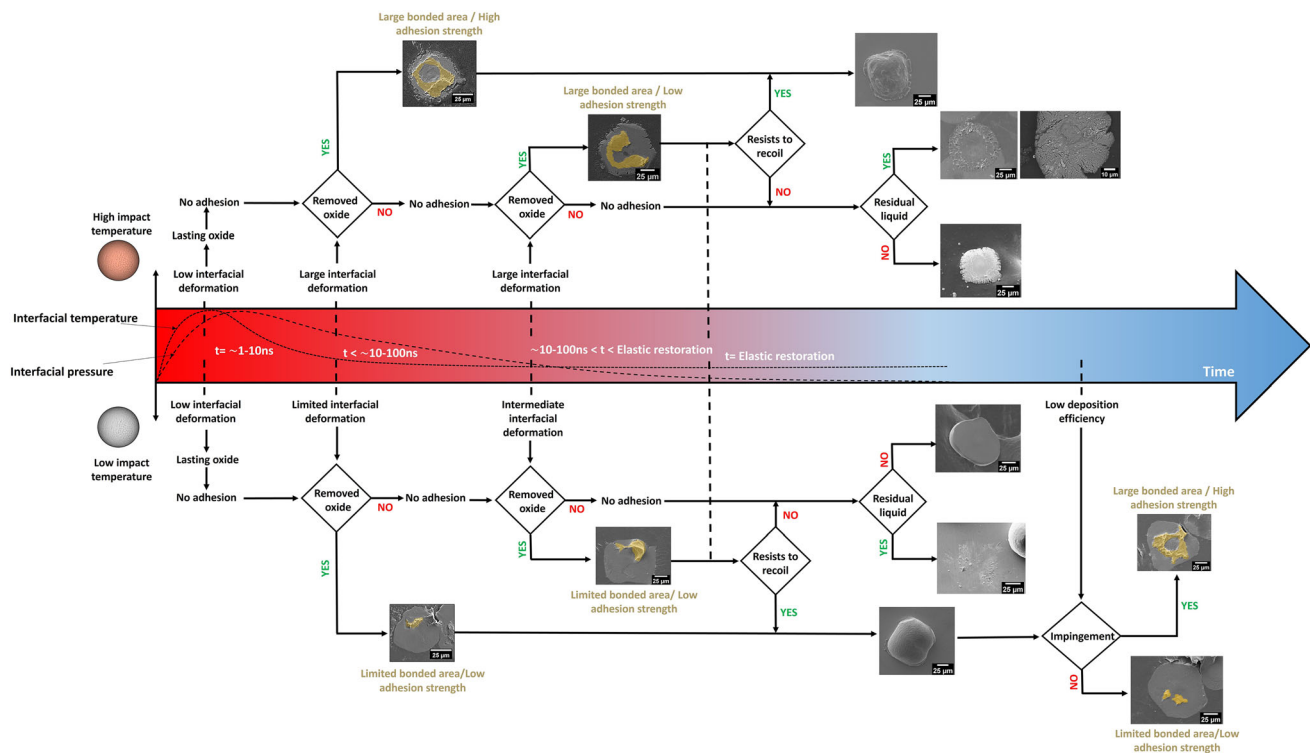


**Fig. 17** Results summary of single particle impact interfacial phenomena based on initial particle temperature (high and low) assuming same particle impact velocity. Interfacial temperature and

compressive contact pressure and surface expansion can, however, be achieved with in situ peening processes which have been shown to be important during LPIT coating deposition (Ref 31).

Aside from in situ peening processes, increasing powder set 3 impact temperature (HPIT conditions) has been shown to increase its  $R_c$ , as demonstrated in Fig. 5, and increase the duration of the zone above melting temperature, as discussed in Particle Melting. This rise in interfacial expansion and decrease in cooling rate, however, lead to the successful deposition of particles traveling at much lower velocity, i.e., lower critical velocity (Ref 31). As particle size increases, the velocity distribution shifts drastically towards lower speeds (Ref 31), which decreases the compressive pressure at the interface and consequently lowers bond strength, as explained through Fig. 15. This low bonding strength has been observed in the HPIT powder set 3 wipe tests, which have shown failure at the particle-to-particle junction.

The pressure and temperature along the interface at 5 ns, 10 ns, 20 ns and 40 ns for both powders set 1 and set 3 sprayed under LPIT condition is illustrated in Fig. 16. The red line separates the unbonded south pole zone with the bonded ring shape regions. The highest pressure and temperature are always reached outside the south pole region

pressure as a function of time are illustrated along with their effect on the resulting adhesion process. Provided experimental observations have been made following particle deposition

and prior to the particle edge/jetting zone, as observed experimentally.

## Summary and Conclusions

This work investigated the interfacial phenomena occurring upon impact of soft aluminum particles on hard steel substrate under low and high particle impact temperatures for similar particle impact velocity to segregate the effect of impact temperature. Three powder size ranges were investigated. The experimental data and impact modeling have shown that adhesion is the result of a complex time-dependent dynamic process. The effect of interfacial deformation, contact pressure and temperature variation with time on the particle bonded area and resulting individual adhesion strength are summarized schematically in Fig. 17. It was found that maximum interfacial pressure and temperature are reached within 3 ns following the particle impact for all cases. Low interfacial deformation, i.e., low surface expansion, during that period ( $t < 3\text{ ns}$ ) prevents proper oxide layer extrusion/removal, impeding the creation of metallic atomic bonds between the incoming particles and the substrate. It was shown that both local interfacial pressures, regulating the adhesion strength, and local temperature, controlling interfacial contact condition,

decrease with time. It was also found that increasing particle impact temperature promotes large interfacial deformation while the local pressure is still elevated ( $t < 15$  ns), leading to high adhesion strength. However, these large interfacial deformations can also lead to lower adhesion strength if they occur too slowly as the localized pressure drops quickly ( $15 < t < \text{elastic restoration}$ ). For low particle impact temperature, although localized high strength bonding can occur while the local pressure is large ( $t < 15$  ns), the overall resulting bond strength is limited/low due to the limited interfacial deformation at lower impact temperature, i.e., limited bonded area. While interfacial deformation can reach intermediate levels ( $15 \text{ ns} < t < \text{elastic restoration}$ ), it nevertheless results in low adhesion strength as the local instantaneous interfacial pressure is significantly lower after 15 ns.

After elastic restoration, rebounded particles reveal large deformation and/or remanent melting features (melt fingers and spheroidal particles) on the substrate surface. The former implies low adhesion strength, improper oxide extrusion, while the latter indicates absence of melt solidification during elastic restoration. Melting occurrence increases with impact temperature and particle size. Lower DE as experienced for the low particle impact temperature case lead to increased in situ impingement processes, which can increase both the interfacial deformation level and local pressure and lead to high adhesion strength even during or after the particle elastic restoration time.

The current study also showed that particle deformation is grain texture dependent, associated with preferred grain orientation with respect to the loading direction. Based on recent molecular single crystal particle impact models, the detected deformations in the current study match results obtained for grains preferentially oriented in the [111], [100] and [110] directions.

**Acknowledgments** This project was funded by the Government of Canada. The authors would like to acknowledge the work of the technical officer's team in Boucherville: K. Bricault, F. Belval, P. Dionne and C. Hoang.

## References

1. P.C. King, C. Busch, T. Kittel-Sherri, M. Jahedi and S. Gulizia, Interface Melding in Cold Spray Titanium Particle Impact, *Surf. Coatings Technol.*, 2014, **239**, p 191–199.
2. G. Bae, S. Kumar, S. Yoon, K. Kang, H. Na, H.J. Kim and C. Lee, Bonding Features and Associated Mechanisms in Kinetic Sprayed Titanium Coatings, *Acta Mater.*, 2009, **57**(19), p 5654–5666.
3. S. Sevsek, C. Haase, W. Bleck, S. Sevsek, C. Haase and W. Bleck, Strain-Rate-Dependent Deformation Behavior and Mechanical Properties of a Multi-Phase Medium-Manganese Steel, *Metals (Basel)*, 2019, **9**(3), p 344. <https://doi.org/10.3390/met9030344>
4. X.T. Luo, C.X. Li, F.L. Shang, G.J. Yang, Y.Y. Wang and C.J. Li, High Velocity Impact Induced Microstructure Evolution during Deposition of Cold Spray Coatings: A Review, *Surf. Coat. Technol.*, 2014 <https://doi.org/10.1016/j.surfcoat.2014.06.006>
5. S. Dosta, G. Bolelli, A. Candeli, L. Lusvardi, I.G. Cano and J.M. Guilemany, Plastic Deformation Phenomena during Cold Spray Impact of WC-Co Particles onto Metal Substrates, *Acta Mater.*, 2017, **124**, p 173–181. <https://doi.org/10.1016/J.ACTAMAT.2016.11.010>
6. M. Hassani-Gangaraj, D. Veysset, K.A. Nelson and C.A. Schuh, Impact-Bonding with Aluminum, Silver, and Gold Microparticles: Toward Understanding the Role of Native Oxide Layer, *Appl. Surf. Sci.*, 2019, **476**, p 528–532. <https://doi.org/10.1016/J.APSUSC.2019.01.111>
7. D. Goldbaum, R.R. Chromik, N. Brodusch and R. Gauvin, Microstructure and Mechanical Properties of Ti Cold-Spray Splats Determined by Electron Channeling Contrast Imaging and Nanoindentation Mapping, *Microsc. Microanal.*, 2015, **21**, p 570–581. <https://doi.org/10.1017/S1431927615000240>
8. A. Nastic, M. Vijay, A. Tieu, S. Rahmati and B. Jodoin, Experimental and Numerical Study of the Influence of Substrate Surface Preparation on Adhesion Mechanisms of Aluminum Cold Spray Coatings on 300M Steel Substrates. *J. Therm. Spray Technol.*, 2017 **26**(7), p 1461–1483.
9. A.P. Semenov, The phenomenon of Seizure and Its Investigation, *Wear, Elsevier*, 1961, **4**(1), p 1–9.
10. H.A. Mohamed, J. Washburn, Mechanism of Solid State Pressure Welding. *Weld. J.* (1975). [http://inis.iaea.org/Search/search.aspx?orig\\_q=RN:8330039](http://inis.iaea.org/Search/search.aspx?orig_q=RN:8330039). Accessed 21 Nov. 2020.
11. S. Rahmati and B. Jodoin, Physically Based Finite Element Modeling Method to Predict Metallic Bonding in Cold Spray, *J. Therm. Spray Technol.*, 2020, **29**(4), p 611–629.
12. A. Nastic, M Vijay, A Tieu, S Rahmati, B Jodoin, Experimental and Numerical Study of the Influence of Substrate Surface Preparation on Adhesion Mechanisms of Aluminum Cold Spray Coatings on 300M Steel Substrates. *J. Therm. Spray Technol.* <https://doi.org/10.1007/s11666-017-0602-1>.
13. W.Y. Li, C.J. Li and H. Liao, Significant Influence of Particle Surface Oxidation on Deposition Efficiency, Interface Microstructure and Adhesive Strength of Cold-Sprayed Copper Coatings, *Appl. Surf. Sci.*, 2010, **256**(16), p 4953–4958.
14. S. Yoon, Y. Xiong, H. Kim and C. Lee, Dependence of Initial Powder Temperature on Impact Behaviour of Bulk Metallic Glass in a Kinetic Spray Process, *J. Phys. D Appl. Phys.*, 2009, **42**, p 5. <https://doi.org/10.1088/0022-3727/42/8/082004>
15. S. Yin, X. Wang, W. Li, H. Liao and H. Jie, Deformation Behavior of the Oxide Film on the Surface of Cold Sprayed Powder Particle, *Appl. Surf. Sci.*, 2012, **259**, p 294–300. <https://doi.org/10.1016/J.APSUSC.2012.07.036>
16. K.H. Kim, W. Li and X. Guo, Detection of Oxygen at the Interface and Its Effect on Strain, Stress, and Temperature at the Interface between Cold Sprayed Aluminum and Steel Substrate, *Appl. Surf. Sci.*, 2015, **357**, p 1720–1726.
17. Y. Xie, S. Yin, C. Chen, M.P. Planche, H. Liao and R. Lupoi, New Insights into the Coating/Substrate Interfacial Bonding Mechanism in Cold Spray, *Scr. Mater.*, 2016, **125**, p 1–4.
18. A. Ganesan, J. Affi, M. Yamada and M. Fukumoto, Bonding Behavior Studies of Cold Sprayed Copper Coating on the PVC Polymer Substrate, *Surf. Coatings Technol.*, 2012, **207**, p 262–269. <https://doi.org/10.1016/J.SURFCOAT.2012.06.086>
19. S. Yin, X. Suo, Y. Xie, W. Li, R. Lupoi and H. Liao, Effect of Substrate Temperature on Interfacial Bonding for Cold Spray of Ni onto Cu, *J. Mater. Sci.*, 2015, **50**(22), p 7448–7457. <https://doi.org/10.1007/s10853-015-9304-6>
20. Y. Xie, C. Chen, M.-P. Planche, S. Deng, R. Huang, Z. Ren and H. Liao, Strengthened Peening Effect on Metallurgical Bonding

- Formation in Cold Spray Additive Manufacturing, *J. Therm. Spray Technol.*, 2019, **28**(4), p 769–779. <https://doi.org/10.1007/s11666-019-00854-4>
21. A. Sabard and T. Hussain, Bonding Mechanisms in Cold Spray Deposition of Gas Atomised and Solution Heat-Treated Al 6061 Powder by EBSD, 2018. <https://arxiv.org/abs/1811.08694>. Accessed 31 Jan 2019
  22. G. Bae, Y. Xiong, S. Kumar, K. Kang and C. Lee, General Aspects of Interface Bonding in Kinetic Sprayed Coatings, *Acta Mater.*, 2008, **56**(17), p 4858–4868.
  23. X.K. Suo, M. Yu, W.Y. Li, M.P. Planche and H.L. Liao, Effect of Substrate Preheating on Bonding Strength of Cold-Sprayed Mg Coatings, *J. Therm. Spray Technol.*, 2012 <https://doi.org/10.1007/s11666-012-9803-9>
  24. Y. Xie, M.P. Planche, R. Raelison, H. Liao, X. Suo and P. Hervé, Effect of Substrate Preheating on Adhesive Strength of SS 316L Cold Spray Coatings, *J. Therm. Spray Technol.*, 2016, **25**(1-2), p 123–130. <https://doi.org/10.1007/s11666-015-0312-5>
  25. W. Sun, A.W.Y. Tan, A. Bhowmik, I. Marinescu, X. Song, W. Zhai, F. Li and E. Liu, Deposition Characteristics of Cold Sprayed Inconel 718 Particles on Inconel 718 Substrates with Different Surface Conditions, *Mater. Sci. Eng. A*, 2018, **720**, p 75–84.
  26. R. Ortiz-Fernandez, S. Imbriglio, R. Chromik and B. Jodoin, The Role of Substrate Preheating on the Adhesion Strength of Cold-Sprayed Soft Particles on Hard Substrates, *J. Therm. Spray Technol.*, 2021 <https://doi.org/10.1007/s11666-020-01148-w>
  27. S. Yin, X. Wang, X. Suo, H. Liao, Z. Guo, W. Li and C. Coddet, Deposition Behavior of Thermally Softened Copper Particles in Cold Spraying, *Acta Mater.*, 2013, **61**(14), p 5105–5118.
  28. C. Chen, X. Xie, Y. Xie, M.-P. Planche, S. Deng, G. Ji, E. Aubry, Z. Ren and H. Liao, Cold Spraying of Thermally Softened Ni-Coated FeSiAl Composite Powder: Microstructure Characterization, Tribological Performance and Magnetic Property, *Mater. Des.*, 2018, **160**, p 270–283. <https://doi.org/10.1016/J.MATDES.2018.09.025>
  29. Y. Xie, M.P. Planche, R. Raelison, P. Hervé, X. Suo, P. He and H. Liao, Investigation on the Influence of Particle Preheating Temperature on Bonding of Cold-Sprayed Nickel Coatings, *Surf. Coatings Technol.*, 2017, **318**, p 99–105.
  30. A. Sova, S. Grigoriev, A. Kochetkova and I. Smurov, Influence of Powder Injection Point Position on Efficiency of Powder Preheating in Cold Spray: Numerical Study, *Surf. Coatings Technol.*, 2014, **242**, p 226–231.
  31. A. Nastic, B. Jodoin, D. Poirier and J.-G. Legoux, Particle Temperature Effect in Cold Spray: A Study of Soft Particle Deposition on Hard Substrate, *Surf. Coatings Technol.*, 2021, **406**, p 126735. <https://doi.org/10.1016/j.surfcoat.2020.126735>
  32. Y. Cormier, P. Dupuis, B. Jodoin and A. Ghaei, Finite Element Analysis and Failure Mode Characterization of Pyramidal Fin Arrays Produced by Masked Cold Gas Dynamic Spray, *J. Therm. Spray Technol.*, 2015, **24**(8), p 1549–1565. <https://doi.org/10.1007/s11666-015-0317-0>
  33. H. Jones, Microstructure of Rapidly Solidified Materials, *Mater. Sci. Eng.*, 1984, **65**(1), p 145–156. [https://doi.org/10.1016/0025-5416\(84\)90208-8](https://doi.org/10.1016/0025-5416(84)90208-8)
  34. A.M. Birt, V.K. Champagne, R.D. Sisson and D. Apelian, Microstructural Analysis of Ti-6Al-4V Powder for Cold Gas Dynamic Spray Applications, *Adv. Powder Technol.*, 2015, **26**(5), p 1335–1347. <https://doi.org/10.1016/J.APT.2015.07.008>
  35. V.S. Bhattiprolu, K.W. Johnson, O.C. Ozdemir and G.A. Crawford, Influence of Feedstock Powder and Cold Spray Processing Parameters on Microstructure and Mechanical Properties of Ti-6Al-4V Cold Spray Depositions, *Surf. Coatings Technol.*, 2018, **335**, p 1–12. <https://doi.org/10.1016/J.SURFCOAT.2017.12.014>
  36. J. Lienhard, C. Crook, M.Z. Azar, M. Hassani, D.R. Mumm, D. Veyssset, D. Apelian, K.A. Nelson, V. Champagne, A. Nardi, C.A. Schuh and L. Valdevit, Surface Oxide and Hydroxide Effects on Aluminum Microparticle Impact Bonding, *Acta Mater.*, 2020, **197**, p 28–39.
  37. H. Skoglund, M.K. Wedel and B. Karlsson, The Role of Oxygen in Powder Processing of FeAl, *Intermetallics*, 2003, **11**(5), p 475–482.
  38. W.Y. Li, H. Liao, C.J. Li, G. Li, C. Coddet and X. Wang, On High Velocity Impact of Micro-Sized Metallic Particles in Cold Spraying, *Appl. Surf. Sci.*, 2006, **253**(5), p 2852–2862.
  39. S. Rahmati and A. Ghaei, The Use of Particle/Substrate Material Models in Simulation of Cold-Gas Dynamic-Spray Process. *J. Therm. Spray Technol.* 530–540 (2014)
  40. M.C. Price, A.T. Kearsley and M.J. Burchell, Validation of the Preston–Tonks–Wallace Strength Model at Strain Rates Approaching  $\sim 1011$  s<sup>-1</sup> for Al-1100, Tantalum and Copper Using Hypervelocity Impact Crater Morphologies, *Int. J. Impact Eng.*, 2013, **52**, p 1–10.
  41. J. Barbour, J. Knapp, D. Follstaedt, T. Mayer, K. Minor and D. Linam, The Mechanical Properties of Alumina Films Formed by Plasma Deposition and by Ion Irradiation of Sapphire, *Nucl. Instruments Methods Phys. Res. Sect B Beam Interact. Mater. Atoms*, 2000, **166–167**, p 140–147. [https://doi.org/10.1016/S0168-583X\(99\)00648-5](https://doi.org/10.1016/S0168-583X(99)00648-5)
  42. S. Shin, S. Yoon, Y. Kim and C. Lee, Effect of Particle Parameters on the Deposition Characteristics of a Hard/Soft-Particles Composite in Kinetic Spraying, *Surf. Coatings Technol.*, 2006, **201**(6), p 3457–3461.
  43. C. Chen, X. Xie, Y. Xie, M.P. Planche, S. Deng, G. Ji, E. Aubry, Z. Ren and H. Liao, Cold Spraying of Thermally Softened Ni-Coated FeSiAl Composite Powder: Microstructure Characterization, Tribological Performance and Magnetic Property, *Mater. Des.*, 2018, **160**, p 270–283.
  44. J. Wu, H. Fang, S. Yoon, H. Kim and C. Lee, The Rebound Phenomenon in Kinetic Spraying Deposition, *Scr. Mater.*, 2006, **54**(4 SPEC. ISS.), p 665–669.
  45. P. Zhao, Q. Zhang, Y. Guo, H. Liu and Z. Deng, Atomic Simulation of Crystal Orientation Effect on Coating Surface Generation Mechanisms in Cold Spray, *Comput. Mater. Sci.*, 2020, **184**, p 109859.
  46. M. Razavipour, S. Rahmati, A. Zúñiga, D. Criado and B. Jodoin, Bonding Mechanisms in Cold Spray: Influence of Surface Oxidation During Powder Storage. <https://doi.org/10.1007/s11666-020-01123-5>.
  47. M. Hassani-Gangaraj, D. Veyssset, V.K. Champagne, K.A. Nelson and C.A. Schuh, Adiabatic Shear Instability Is Not Necessary for Adhesion in Cold Spray, *Scr. Mater.*, 2018, **158**, p 430–439.
  48. H. Assadi, F. Gärtner, T. Stoltenhoff and H. Kreye, Bonding Mechanism in Cold Gas Spraying, *Acta Mater.*, 2003, **51**(15), p 4379–4394.
  49. M. Grujcic, C. Zhao, W. DeRosset and D. Helfritsch, Adiabatic Shear Instability Based Mechanism for Particles/Substrate Bonding in the Cold-Gas Dynamic-Spray Process, *Mater. Des.*, 2004, **25**(8), p 681–688.
  50. M.P. Dewar, A.G. McDonald and A.P. Gerlich, Interfacial Heating during Low-Pressure Cold-Gas Dynamic Spraying of Aluminum Coatings, *J. Mater. Sci.*, 2012, **47**(1), p 184–198. <https://doi.org/10.1007/s10853-011-5786-z>
  51. A. Dorogoy and D. Rittel, Determination of the Johnson–Cook Material Parameters Using the SCS Specimen, *Exp. Mech.*, 2009, **49**(6), p 881–885. <https://doi.org/10.1007/s11340-008-9201-x>
  52. A. Hännström and P. Lazor, High Pressure Melting and Equation of State of Aluminum, *J. Alloys Compd.*, 2000, **305**(1-2), p 209–215.

53. S. Chandra and P. Fauchais, Formation of Solid Splats During Thermal Spray Deposition, *J. Therm. Spray Technol.*, 2009, **18**(2), p 148–180. <https://doi.org/10.1007/S11666-009-9294-5>
54. C.-J. Li, C.-X. Li, G.-J. Yang and Y.-Y. Wang, Examination of Substrate Surface Melting-Induced Splashing during Splat Formation in Plasma Spraying, *J. Therm. Spray Technol.*, 2006, **15**(4), p 717–724. <https://doi.org/10.1361/105996306X146947>
55. A. Ranjan, A. Islam, M. Pathak, M.K. Khan and A.K. Keshri, Plasma Sprayed Copper Coatings for Improved Surface and Mechanical Properties, *Vacuum, Pergamon*, 2019, **168**, p 108834.
56. M. Hassani, D. Veysset and C.A. Schuh, Melting Can Hinder Impact-Induced Adhesion, *Artic. Phys. Rev. Lett.*, 2017 <https://doi.org/10.1103/PhysRevLett.119.175701>
57. X. Song, J. Everaerts, W. Zhai, H. Zheng, A.W.Y. Tan, W. Sun, F. Li, I. Marinescu, E. Liu and A.M. Korsunsky, Residual Stresses in Single Particle Splat of Metal Cold Spray Process—Numerical Simulation and Direct Measurement, *Mater. Lett.*, 2018, **230**, p 152–156.
58. T. Schmidt, H. Assadi, F. Gärtner, H. Richter, T. Stoltenhoff, H. Kreye and T. Klassen, From Particle Acceleration to Impact and Bonding in Cold Spraying, *J. Therm. Spray Technol.*, 2009, **18**(5-6), p 794–808. <https://doi.org/10.1007/s11666-009-9357-7>
59. K. Binder, J. Gottschalk, M. Kollenda, F. Gärtner and T. Klassen, Influence of Impact Angle and Gas Temperature on Mechanical Properties of Titanium Cold Spray Deposits, *Journal of Thermal Spray Technology*, 2011 <https://doi.org/10.1007/s11666-010-9557-1>
60. N. Bay, Mechanisms Producing Metallic Bonds in Cold Welding, *Weld. J.*, 1983, **62**(5), p 137.
61. S. Kumar, B.R. Bodapati, G. Vinay, K. Vamshi Kumar, N.M. Chavan, P. Suresh Babu, and A. Jyothirmayi, Estimation of Inter-Splat Bonding and Its Effect on Functional Properties of Cold Sprayed Coatings, *Surf. Coatings Technol.*, Elsevier, 2021, **420**, p 127318.

**Publisher's Note** Springer Nature remains neutral with regard to jurisdictional claims in published maps and institutional affiliations.